Article:

He, Q., Shi, K., Ma, Y. et al. (2025) Evolution of rimmed carbonate platform architecture controlled by sea-level change: Insights from the Lower-Middle Cambrian of the Northern Tarim Basin, China. Marine and Petroleum Geology, 171. 107215. ISSN: 0264-8172

https://doi.org/10.1016/j.marpetgeo.2024.107215

Evolution of rimmed carbonate platform architecture controlled by sea-level change: insights from the Lower-Middle Cambrian of the Northern Tarim Basin, China

Qing He[1], Kaibo Shi[1*], Yongsheng Ma[1], Bo Liu[1*], Jun Han[2], Jun Li[1], Xiangyu Bai[1], Chun Wu[1], Adam D. McArthur[3] and Nigel P. Mountney[3]

[1]School of Earth and Space Sciences, Peking University, Beijing, 100871, China
[2]Northwest Oilfield Company, Sinopec, Urumqi, 830111, China
[3]Institute of Applied Geosciences, University of Leeds, Leeds, LS2 9JT, UK

Abstract

The sedimentary architecture of carbonate platforms is determined by distinct paleobiological, tectonics, climatic, oceanic and environmental conditions. During the Cambrian period, a rimmed carbonate platform system developed over an area of ~28 $\times 10^4$ km^2 in the Tarim Basin. However, the evolution mechanism and its predominant controlling factors remain poorly understood. The investigation utilized integrated analysis of cores, thin sections, 3-D seismic, well logging and geochemical data to explain the sequence stratigraphic framework, depositional architecture and main controlling factors. Sixteen distinct microfacies (MF1–MF16) are identified based on thin-section analysis of the five lithofacies, which could be further grouped into fourteen microfacies associations (MA1-MA14). These fourteen microfacies associations respectively represent fourteen facies belts of the five facies of the shelf, outer ramp, middle ramp, platform margin and restricted platform. Microfacies and seismic characteristics have provided the basis for establishing a sequence-stratigraphic framework. Two regionally extensive second-order sequences (CS1-CS2) are developed in the Lower-Middle Cambrian succession; CS1 incorporates five third-order sequences (Sq1-Sq5); CS2 incorporates three third-order sequences (Sq6-Sq8). The lateral migration and vertical arrangement of depositional facies resulted in a unique depositional architecture. The overall carbonate platform architecture is interpreted from 3D seismic data, integrated with the depositional facies interpretations to document the evolution of the depositional setting over time from a broad shelf (Sq1-Sq2), to a distally steepening ramp (Sq3-Sq4), to a weekly rimmed platform (Sq5), and finally to a strongly rimmed platform (Sq6-Sq8). Relative sea-level (RSL) curves were reconstructed through an integrated analysis of Fischer plots from three wells. The determined RSL curve matches closely with reconstructed paleo-water depths indicated by the distribution of microfacies types. The inferred paleo-water depths changes comprise two long-term shallow–deep–shallow trends, upon which eight intermediate-term cycles are superimposed. Microfacies also have been applied to explain the evolution of the platform in response to RSL change and other environmental factors. A major transgression occurred in the lower parts of CS1.

Results demonstrate that RSL and paleo-water depth changes in the Lower-Middle Cambrian are consistent with known global sea-level changes indicated by geochemical elements. The architectural and sequence-stratigraphic evolution of the progradational rimmed carbonate platform was controlled principally by eustasy. This study is important due to the limited information on Cambrian rimmed platforms.

Key words: Cambrian, microfacies, sequence stratigraphy, platform architecture, sea-level change, Tarim Basin

1. Introduction

Carbonate platforms develop and grow principally in response to changes in biology, carbonate productivity, tectonics, climate, allochthonous sediment input, and eustasy (Heldt et al., 2010; Phelps et al., 2014; Pomar et al., 2015; Pomar et al., 2004; Scott et al., 1993; Yu et al., 2011). The margins of many rimmed carbonate platforms are sites of reef-shoal accumulation, and such stratal bodies form important reservoir units that host various resources of economic significance (Castro et al., 2008; Gao and Fan, 2015; Graziano, 2000; Santantonio et al., 2013; Zhu et al., 2015; Wang et al., 2024; Wang et al., 2025). The highly diverse carbonate factories and changes in accommodation space driven by sea-level rise and regional tectonics add significant complexity to seismic interpretation, sedimentological analysis, and hydrocarbon exploration (Markello et al., 2008; Wright and Burgess, 2005). Different types of carbonate factories have distinct carbonate sediment production rates, depth distributions, and grain sizes, which significantly impact the geometric morphology of carbonate platforms (Pomar and Hallock, 2008; Schlager, 2003). Sea-level fluctuations play a crucial role in determining spatiotemporal evolutionary processes and facies distributions within carbonate platforms (Wagner et al., 2004). However, in specific tectonic settings, such as where carbonate platforms develop rotational fault-blocks, the changes in accommodation space generated by tectonics can override the eustatic effect (Bosence et al., 1998).

After Ordovician, the rimmed carbonate platform margins were characterized by reefs built by corals and certain species of clams, which serve as barriers that drastically reduce wave energy (Xu et al., 2023). Prior to the Ordovician, the general absence of macroscopic reef-building organisms and the abundance of micro-organisms acted to limit the scale and extent of many platform-margin systems (Wood et al., 2019; Zhuravlev and Wood, 2018). Globally, few distinct rimmed carbonate platforms developed during the Ediacaran-Cambrian period. During the Cambrian, large-scale reef-shoals that apparently migrated continuously and rapidly under the influence of wave and tidal currents accumulated on carbonate platform margins in the Tarim Basin (Huang et al., 2020). The paleogeographic and spatiotemporal evolution of these Cambrian platform margins has been the focus of several studies in recent years. Importantly, the scheme for the stratigraphic subdivision in the platform margin remains uncertain due to the chaotic nature of the seismic reflections in this region. Gao and Fan (2015) and Huang et al. (2020) identified depositional evolutionary processes within two sedimentary settings: ramp and rimmed platform. These authors delineated the zone of platform-margin development via interpretation of seismic reflection profiles. Zhang et al. (2021) identified the stages of evolution of the reef-shoal on the Cambrian platform margin and reconstructed the paleogeomorphology within the marginal zone. However, the main factors controlling the evolution of the Cambrian carbonate platforms of the Tarim Basin, and the drivers of the proliferation and widespread accumulation of platform-margin reef-shoals, remain unclear.

In this study, we utilise a subsurface dataset of 3D seismic, wireline well logs, core, petrographic and geochemical data to investigate the evolution process and main controlling factor of the Cambrian carbonate platforms of the Tarim Basin. The Lower-Middle Cambrian sequence stratigraphic framework and the evolutionary trends of the rimmed carbonate platform are established by detailed analysis of microfacies and their associations. An integrated analysis of Fischer plots obtained by continuous wavelet transformation, carbon and oxygen isotopes, and microfacies allows for the reconstruction and comparison of paleo-water depth and sea-level changes. Importantly, this study discusses the influences of paleocurrent directions, tectonic activity, global sea-level changes, and changes in other environmental controlling factors on the Cambrian rimmed platform evolution in the Tarim Basin. Results provide valuable insights into the processes acting upon and controlling Ediacaran-Cambrian rimmed carbonate platform development more generally.

2. Geological setting

The Tarim Basin is a sedimentary basin (56×10^4 km^2) located in northwest China (Fig. 1a). It is bordered by the Kunlun-Altyn Mountains of the Tethys system to the south, and by the Tianshan Mountain of the Paleo-Asian system to the north (Fig. 1b; Lin et al., 2011). In the Neoproterozoic, the Tarim Basin was affected by extension due to the break-up of the Rodinia Supercontinent (Huang et al., 2005). During the Ediacaran-Cambrian transition period, the “Snowball Earth” event, characterized by extreme glaciation, impacted the climate and sedimentary processes in the Tarim Basin (Shang et al., 2020). During the Cambrian, "Cambrian explosion" occurred, known as a rapid diversification of life forms. This biological event had a significant impact on the marine environments, as the proliferation of life influenced the types of sediments being deposited (Servais et al., 2023). The Tarim Basin was located in a low-latitude zone near the equator that suggests a hot and arid climate for the region (He et al., 2016). The depositional paleogeomorphology of the basin was controlled by late Ediacaran tectonic activity (Ge et al., 2014; Li et al., 2013; Shi et al., 2018), and featured three uplifts: the Lunnan-Yaha Uplift, Keping-Wensu Uplift and southwestern Uplift; these were separated by two depressions developed between them (Zhu et al., 2019). The Early Cambrian syn-sedimentary structures in northern Tarim Basin mainly include syn-sedimentary faults (Gao et al., 2022; Guan et al., 2019; Yang et al., 2017). Hereafter, in response to gradual tectonic subsidence, the paleogeographic framework slowly changed, whereby a paleo-high developed in the west and a paleo-low developed in the east of the Tarim Basin (Fig. 2; Wei et al., 2021). During the Phanerozoic, multiple episodes of tectonic activity and deformation associated with the Caledonian, Hercynian, Indosinian, and Himalayan orogenies transformed the Tarim Basin into a superposed complex basin with a Mesozoic–Cenozoic foreland cover overlying the earlier Paleozoic intracratonic basin fill (Jia, 1999). This study focuses on the Tabei Uplift in the northern Tarim Basin (Fig. 1b), which is situated at the periphery of the Lunnan-Yaha Uplift.

The Cambrian succession is characterized by several distinct carbonate sedimentary systems. Together, these record evidence of a transition from a shallow-water marine to a deeper basinal setting (Fig. 2 andFig. 3). Taking the Lunnan-Gucheng platform margin zone as the line of demarcation (Cao et al., 2018; Ni et al., 2015; Yan et al., 2018), strata of Cambrian are divided into three major packages, each located in a distinct sub-region; each representing a different paleoenvironment in the Tarim Basin (Jiang et al., 2021b). The platform interior and the platform margin are located in the western part of the Tarim Basin, whereas the basinal region is located in the eastern Tarim Basin (Fig. 1b; Feng et al., 2006). The platform margin is the transitional region between the shallow-water platform and the deeper-water basin.

The Lower Cambrian succession comprises the Yuertusi, Xiaoerbulake and Wusonggeer Formations. The Yuertusi Formation is composed of organic-rich argillite (Chen et al., 2015a; Chen et al., 2015b). The Xiaoerbulake Formation is composed of micitic dolomite, microbial dolomite and dolo-grainstone in the western platform zone (Jiang et al., 2021b), whereas it is composed of micitic limestone and dolomitic limestone in the eastern platform zone, and contains argillite in the basin zone (Hu et al., 2019). The Wusonggeer Formation is composed of argillaceous dolomite, gypsum dolomite and evaporite in the western platform zone, whereas it is composed of microbial dolomite and dolo-grainstone in the eastern platform zone, and contains argillite and carbonaceous mudstone in the basin zone (Bai et al., 2019). The Middle Cambrian succession comprises the Shayilike and Awatage Formations, which are composed of deposits dolo-grainstone and microbial dolomite in the eastern platform zone, and of argillite in the basin zone (Gao and Fan, 2015). However, in the western platform zone, the Shayilike Formation is composed of micritic limestone, whereas Awatage Formation is dominantly composed of argillaceous dolomite and evaporate (Zhang et al., 2023).

3. Data and methods

The present study is based on data from five wells Y1, Y2, Y3, Y4 and Y5 penetrating or drilling the Lower-Middle Cambrian succession with thickness of 1123.5 m, 1034.5 m, 856 m 1087.5 m and 884 m, respectively, and 3-D seismic dataset in the Tabei Uplift of the Tarim Basin. The well-logging data studied include natural gamma ray logs. Detailed observations and descriptions were made from 2749 thin sections of drill cutting from five wells (Y1, Y2, Y3, Y4 and Y5) and 40 thin sections of 222 cores with a cumulative length of 59.49 m from three wells (Y1, Y4 and Y5). The thin sections of cuttings were sampled at one-meter (wells Y1 and Y4) and five-meter (wells Y2, Y3 and Y5) intervals.

The study of microfacies was based primarily on the analysis of cores and thin sections (Fig. 4 and Fig. 5). The classification of microfacies was dependent on the identification of depositional and diagenetic fabric, grain type, biological allochem type, and matrix type in the thin sections (*sensu* Flügel, 2010). Based on Dunham's (1962) carbonate classification system, the abundance of argillaceous components, gypsum content and diverse types of grains and fossils were determined visually using a polarizing microscope. The proportions of individual microfacies types in the microfacies associations were depicted on stacked bar charts (Fig. 6 and Fig. 7). From this, four measures of relative abundance were defined: abundant (>50%), frequent (25–50%), less common (10–25%), and rare (<10%). By combining data studied herein with the research results of Wilson (1975) and Flügel (2010) on microfacies and microfacies associations, the characteristics of the depositional facies were analyzed and established.

The stratal stacking patterns of microfacies units and their associations thereof were determined and checked via calibration of well data and 3-D seismic profiles. These data were used to identify sequence boundaries and to establish a sequence-stratigraphic framework. Sequence stratigraphic interpretations were made to constrain the stacking patterns of depositional architectural units (Catuneanu et al., 2009). Fischer plots constructed from the 5 studied wells were drawn based on a recognition of high-frequency cycles via analysis of continuous wavelet transform of the gamma-ray logging data (cf. Yu et al., 2022). For the analysis of carbon and oxygen isotopes, the cutting samples were reacted with anhydrous phosphoric acid and the purified CO_2 was tested by a Thermo MAT-253 mass spectrometer at Beijing Research Institute of Uranium Geology. Microfacies, microfacies associations, Fischer plots, and carbon and oxygen isotopes were interpreted to reconstruct a history of paleo-water depth and relative sea-level changes (Geyman et al., 2021; Naderi-Khujin et al., 2020; Zadeh and Shafeii, 2021).

4. Results

4.1. Microfacies characteristics and environment interpretation

Based on observations and comprehensive analysis of thin sections, five lithofacies types (argillite, argillaceous carbonate, carbonate, gypsum carbonate and evaporite) can be divided into sixteen microfacies (MF1-MF16; Fig. 4 and Fig. 5), including argillite (MF1), argillaceous carbonate (MF2 and MF9), carbonate (MF3-MF8 and MF10-MF14), gypsum carbonate (MF15) and evaporite (MF16). Different microfacies were deposited under different hydrodynamic conditions and depositional environments. A summary of the identifying characteristics of each of these microfacies and their occurrence in microfacies associations is presented in Table 1.

4.2. Microfacies associations characteristics and depositional facies

To characterize the local depositional environments in more detail, the characteristics of combinations of microfacies that occur in vertical successions as microfacies associations have been studied. Based on their relative abundance and order of vertical stacking, microfacies were assigned to 14 distinct microfacies associations (MA1-MA14), each of which is interpreted to record different depositional facies in the study area (Fig. 6 and Fig. 7). Vertical facies successions are commonly arranged into repeating meter-scale cycles; the internal facies composition and arrangement of these cycles is described in the sections that follow.

4.2.1. Shelf Facies Association (MA1-MA2)

4.2.1.1 MA1- Deep shelf

Composition: MA1 is characterized by the abundant presence of MF1 (A), the frequent presence of MF2 (F), the less common presence of MF3 (C), and the rare presence of MF4 (R; Fig. 6a). MF1 is rich in black organic asphalt, containing siliceous spicules (Fig. 4a). The mud in MF2 exhibits a zonal distribution (Fig. 4b). The meter-scale cycles formed by MA1 generally contain MF1 in their lower part, and MF2 in their upper part (Fig. 6b). MA1 is developed in the lower Yuertusi Formation, with a total thickness of ~25-35 m (Fig. 8). Vertically, MA1 commonly grades upward into MA2.

Interpretation: MA1 records deposition in a very low- to low-energy setting. The large amount of organic asphalt in the argillite indicates that these deposits accumulated in a reducing depositional environment (Jiang et al., 2021a; Zhou et al., 2015). Sponge spicules indicate 100-200m deep-water conditions (Beauchamp and Grasby, 2012; Wang et al., 2021). In addition, MA1 is widely distributed and changes rapidly longitudinally, likely indicating that it formed in response to rapid marine transgression (Lin et al., 2008). Collectively, these features suggest that MA1 was deposited in a deep shelf environment.

4.2.1.2 MA2- Shallow shelf

Composition: MA2 is characterized by MF3 (A), MF6 (F), MF2 (R) and MF4 (R). Calcite and dolomite in MF6 are distributed in patches (Fig. 4h). Eighty per cent of the MF3 is present in the lower part of the meter-scale cycles formed by MA2 (Fig. 4c), and MF6 is developed in the upper part (Fig. 6c). MA2 occurs commonly in the Tabei Uplift, and is developed in the upper Yuertusi Formation, with a total thickness of ~15-35 m (Fig. 9).

Interpretation: The dominance of MF3 and MF6 in MA2 indicates accumulation in a low-energy depositional environment. The presence of MF6 reveals that the water depth was shallow (Montanez and Read, 1992; Noorian et al., 2022). In addition, the meter-scale cycles of MA2 overlie the deposits of MA1. Based on the superposition of microfacies associations, MA2 was deposited in a shallow-marine shelf environment.

4.2.2. Ramp Facies Association (MA3-MA7)

4.2.2.1 MA3- Outer ramp

Composition: MA3 is characterized by MF3 (A), MF4 (C), MF6 (C) and MF2 (R). In addition, vertically, MA3 normally overlays MA2. The bottom parts of the meter-scale cycles formed by MA3 are dominated by MF3, whereas the top is characterized by the development of MF4 (Fig. 6d).

MA3 occurs mainly in well Y4, and is developed in the lower Xiaoerbulake Formation with a total thickness of ~50 m (Fig. 10).

Interpretation: the dominant occurrence of MF3 in MA3 indicates a low-energy depositional environment (Osleger, 1991). Less common MF4 and rare MF6 indicate a relatively deep environment. The small thickness of MA3 in the east and its restricted distribution in the study area indicate that the depositional environment was relatively deep and the sediment supply was low (Pomar et al., 2005). Collectively, these features suggest that MA3 was deposited in an outer ramp setting.

4.2.2.2 MA4-Outer middle ramp

Composition: MA4 is characterized by MF4 (A), MF6 (F), MF3 (C) and MF5a (R). Part of MF6 was formed after the dolomitization of MF4, and most of MF3 has been subject to recrystallization with very fine calcite. Vertically, MA4 overlays MA3. The meter-scale cycles formed by MA4 generally contain MF3 at the bottom and MF4 (Fig. 5e) in the lower part of the cycle. The upper part of the cycle is characterized by MF6. MA4 is developed to the west of MA3 and occurs mainly in wells Y1, Y2 and Y3 with a total thickness of ~150-370 m (Fig. 8 and Fig. 9).

Interpretation: MF4 indicates a low- to moderate-energy depositional environment (Tucker, 1990). The proportion of MF4 and MF6 is more than 75% of the total in MA4, which is greater than their proportions in MA3 (20%; Fig. 6a). This indicates that MA4 was deposited in shallower water than MA3 and the sediments were more occasionally susceptible to current influence (Bosence et al., 2000). MA4 was likely deposited in the outer part of the middle ramp.

4.2.2.3 MA5- Inner middle ramp

Composition: MA5 is characterized by MF6 (A), MF7 (F), MF4 (C), MF3 (R) and MF5 (R). Calcite in MF7 is dispersed within dolomite (Fig. 4i). Vertically, MA5 overlays MA4. The bottom of the meter-scale cycles formed by MA5 is dominated by MF4. The lower part contains MF6, whereas the upper part contains a large set of MF7 (Fig. 6f). MA5 occurs mainly in well Y1, and is developed in the middle-upper Xiaoerbulake Formation (Fig. 8).

Interpretation: the dominance of MF6 and MF7 suggests that MA5 is developed in a low-energy depositional environment. The occurrence of MF7 indicates MA5 accumulated in a shallower-water setting than MA4. The observed features and relationships suggest that MA5 was deposited in the inner part of the middle ramp.

4.2.2.4 MA6- Lagoon of middle ramp

Composition: MA6 is characterized by MF6 (A), MF9b (F), MF4 (F), MF7 (C), MF5 (C), and MF3 (R). Thin layers of MF5b (3-5 cm thick) are distributed in MA6. The bottommost parts of the meter-scale cycles formed by MA6 are dominated by MF6. The lower part contains MF4 and MF5 (Fig. 4e and Fig. 4f), whereas the upper part contains a large set of MF7 and MF9 (Fig. 6g). MA6 occurs mainly in well Y1 and is developed in the upper part of the Xiaoerbulake Formation with a total thickness of ~120 m. Laterally, MA6 is developed to the west of MA7 (Fig. 8).

Interpretation: The occurrence of 70% of MF6 and MF9b in the MA6 indicates that the environment was low- to moderate energy and restricted, likely in a proximal middle ramp setting.

MF5b is developed in the strata with thin layers, revealing the intermittent occurrence of storms (Scholle and Ulmer-Scholle, 2003). MF5b indicates a shallow-water, high-energy environment (Flügel, 2010). The variety of microfacies present in this environment was likely due to a variable water energy regime. Collectively, these features suggest that MA6 was deposited in a lagoon of a middle ramp environment.

4.2.2.5 MA7- Shoal of middle ramp

Composition: MA7 is characterized by MF5 (A), MF13 (F), MF7 (C) and MF6 (C). MF5 is composed of ooid and sand-sized intraclasts with partial dolomitization (Fig. 4g). MF13 preserves a residual phantom of its original structure (Fig. 5f). Vertically, MA7 overlies MA5. In the lower part of the meter-scale cycles formed by MA7, MF5a and MF5c are developed. MF13 is commonly observed in the upper part (Fig. 6h), which is mainly present in well Y2 and is developed to the east of MA6; typical thickness ~100 m (Fig. 9).

Interpretation: MF13 and MF5, with sparite cement, are interpreted to be typical sediments in shallow-water, medium-to-high-energy environments (Elrick and Read, 1991). Previous studies suggested that sea-floor topography (i.e., local relief) and sea level jointly act to control the location of high-energy shoals, whereby small changes in seabed topography might lead to conditions favorable for the development of shoals (Burchette and Wright, 1992). MA4 is considered to be a shoal deposit of the middle ramp environment.

4.2.3. Semi-restricted to restricted platform Facies Association (MA8-MA12)

4.2.3.1 MA8- Muddy dolomite flat

Composition: MA8 is characterized by MF9 (A), MF8a (F), MF10 (C) and MF15 (R). The mud is mostly distributed in a lamellar form in MF8a (Fig. 4j). Vertically, MA5 overlays MA4. The meter-scale cycles formed by MA8 generally contain MF9 and MF8a in the lower part (Fig. 7b). MA8 occurs mainly in well Y1 and is developed in Wusonggeer and Awatage formations with a total thickness of ~40-60 m (Fig. 8).

Interpretation: MA8 is dominated by MF8a and MF9 and was deposited in a shallow-water and low-energy depositional environment (Lai et al., 2021; Longhitano et al., 2012). The laminated mud is interpreted as a tidal flat deposit in a restricted environment (Daidu et al., 2013). These features suggest that MA8 was deposited in the muddy dolomite flat area of a restricted platform.

4.2.3.2 MA9- Dolomite flat

Composition: MA9 is characterized by MF8b (A), MF8a (F), MF10 (F) and MF8c (C). MF9a developed argillaceous laminae (Fig. 4k). Microcrystalline dolomite has semi-planar-s and planar-s crystal structure characteristics (Fig. 4l). Ten per cent of MF8c is developed in MA9 (Fig. 5a). Thirty per cent of MF8a is present in the lower part of the meter-scale cycles formed by MA9, and MF8b is developed in the upper part (Fig. 7c). MA9 occurs mainly in the Shayilike Formation (wells Y1 and Y2; Fig. 8 and Fig. 9) and in the upper Awatage Formation (wells Y3, Y4 and Y5) with a thick thickness of ~40-80 m (Fig. 10).

Interpretation: MA9 is mainly composed of MF8a and MF8b, indicating that it was deposited in a low-energy and restricted environment (Hsu and Siegenth. C, 1969; Huang et al., 2009). The absence of mud and grains is suggestive of an open-water setting. Therefore, MA9 is considered as a dolomite flat deposit of semi-restricted platform environment.

4.2.3.3 MA10- Gypsum-dolomite flat

Composition: MA10 is characterized by MF15 (A), MF9 (F), MF8b (C), MF11 (R) and MF16 (R; Fig. 5l). The anhydrite nodules/agglomerates inside MF15 are isolated, or are connected laterally in the chicken-wire shape and filled in the water shrinkage joints produced by mud cracking (Fig. 5k). Vertically, MA10 overlays MA9. The bottom of the meter-scale cycles formed by MA10 is dominated by MF9, whereas the top is characterized by the development of MF15 (Fig. 7d). MA10 occurs mainly in wells Y1 and Y2; it is developed in Wusonggeer and Awatage formations (Fig. 8 and Fig. 9).

Interpretation: MA10 is dominated by MF15 and MF9 deposited in a low-energy depositional environment. MF15 indicates a restricted evaporate tidal flat with high salinity (Zhong et al., 2022). The alternating occurrence of MF15 and MF9 reveals that the succession was influenced by daily changes of water level in the tidal flats (Diedrich, 2002; Herrmann et al., 2018; Yoshida et al., 2004). Collectively, these features suggest that MA10 was deposited in the gypsum-dolomite flat of a restricted platform.

4.2.3.4 MA11- Inner shoal

Composition: MA11 is characterized by MF13 (A), MF12b (F), MF8a (F), MF8b (F) and MF10 (R). MF12b has relatively poor sorting (Fig. 5e). The lower part of the meter-scale cycles formed by MA11 is dominated by MF8a and MF8b, whereas the upper part contains a large set of MF13 intercalated with MF12b (Fig. 7e). MA11 occurs in Shayilike Formation (well Y2; Fig. 9) and upper Awatage Formation (wells Y4 and Y5; Fig. 10).

Interpretation: The dominant composition and intercalation of MF13, MF12b and MF8 in MA11 indicates rapid energy changes in a marine environment (Liu et al., 2020). MF12b reveals a high-energy environment without sufficient elutriation by water (Gao et al., 2015; He et al., 2017). The interior of MA8 and MA10 indicate a relatively open and moderate-energy environment. Based on the superposition of microfacies associations, MA7 was deposited in the inner shoal of semi-restricted platform.

4.2.3.5 MA12- Inner mound

Composition: MA12 is characterized by MF14a (A), M8b (F), MF10 (C) and MF13 (C). The meter-scale cycles formed by MA12 generally contain M8b in the lower part of the cycle. The upper part is characterized by MF14a (Fig. 7f). MA12 occurs mainly in wells Y4 and Y5 in the upper Awatage Formation (Fig. 10).

Interpretation: The dominant composition of MF14a and MF8b in MA12 indicates deposition in a shallow-water, moderate- to high-energy depositional environment, similar to MA11. MA12 occurs close to MA11 and the development of both MA12 and MA11 was likely controlled by locally elevated paleo-relief (Ren et al., 2023; Tan et al., 2022). MA12 is considered to represent inner mound deposits of a semi-restricted platform.

4.2.4. Platform margin Facies Association (MA13-MA14)

4.2.4.1 MA13- Margin mound-shoal complex

Composition: MA13 is characterized by MF14a (A; Fig. 5g), MF14b (A; Fig. 5h), MF12 (F), MF13 (F), MF10 (C), MF11 (C; Fig. 5c) and MF14c (C; Fig. 5i). MF14b is present at the bottom of the meter-scale cycles formed by MA13. MF14a and MF13 can be observed in the lower part and MF14c and MF12 are observed in the upper part (Fig. 7g). MA13 occurs mainly in well Y2, Y3, Y4 and Y5 in the eastern platform in the Wusonggeer Formation and Middle Cambrian (Fig. 9 and Fig. 10).

Interpretation: MA13 is mainly developed in the platform margin; MF12, MF13, and MF14 collectively indicate a shallow-water and moderate-to-high energy depositional environment. The interactive development characteristics of MF12 and MF14 reveals changes in water energy from moderate to high (James and Vonderborch, 1991; Rosenau et al., 2012). The large proportion of clasts of microbial origin indicates that MA13 is a mound-shoal complex deposit located on the platform margin.

4.2.4.2 MA14- Margin shoal

Composition: MA14 is characterized by MF12a (A; Fig. 5e), MF12b (F), MF13 (F; Fig. 5f) and MF10 (C; Fig. 5b). MF12a is internally characterized by concentric growth structures (Fig. 5d). Vertically, MA14 overlays MA13, and in places alternates development with MA13. In the lower part of the meter-scale cycles formed by MA7, MF10 and MF13 is developed, whereas MF12a and MF12b tend to be present in the upper part (Fig. 7h). MA14 occurs mainly in wells Y2, Y3, Y4 and Y5 in the eastern part of the platform and is accompanied by MA13 (Fig. 9 and Fig. 10).

Interpretation: The presence of intergranular sprite cement in MF12 indicates that it was formed in a high-energy marine depositional environment (Elrick and Read, 1991). The high degree of particle sorting and rounding of grains in MF12 indicates formation after sufficient elutriation (Xi et al., 2017). The increase in dolo-grainstone content in MA14 indicates a depositional environment that was shallower than MA13. Therefore, MA14 is considered as a platform margin shoal deposit.

4.3. Sequence stratigraphy

The sequence stratigraphic framework for the Lower-Middle Cambrian succession in the study area has been established via integrated analyses of microfacies, stacking patterns of stratal packages composed of the various microfacies associations, and regional tracing of key reflections on the seismic data sets. The Lower-Middle Cambrian succession can be divided into two scales (cf. Catuneanu, 2019; Embry, 1993) of stratigraphic units: 2nd-order sequences within which 3rd-order sequences occur superimposed. In carbonate depositional systems, lowstand and falling stage systems tracts are poorly developed. Herein, an upward-deepening transgressive systems tract (TST) and upward-shallowing regressive systems tract (RST) terminology has been used to subdivide the 3^{rd}-order sequences. Subaerial unconformities and maximum flooding surfaces (MFS) are identified; these are used to define sequence boundaries and systems tract boundaries, respectively (Catuneanu, 2019; Catuneanu et al., 2006; Embry, 1993). Moreover, upward variations in stratal stacking patterns may also record transitions between systems tracts (Chen et al., 2001; Cloyd et al., 1990; Gil et al., 2006; Goldhammer et al., 1990; Osleger and Read, 1991).

In this study, the Lower-Middle Cambrian succession is divided into two 2^{nd}-order sequences (CS1 and CS2; Fig. 14 and Fig. 15), both of which incorporate regional transgressive and regressive cycles. Sequences CS1 and CS2 are delineated by three 2^{nd}-order megasequence boundaries (Msb): Msb1 (bottom of Lower Cambrian succession); Msb2 (top of Lower Cambrian succession); and Msb3 (top of Middle Cambrian succession).

Msb1 is represented by a large-scale regional unconformity in outcrops in the north-western Tarim Basin; this surface is associated with a distinctive karst breccia at the top of the Ediacaran (Gao et al., 2022; Zhao et al., 2011). In Well Y2, the interpreted depositional environment changes from tidal flat of an inner ramp below the surface (Chen et al., 2023), to deep shelf facies above the surface, with the microfacies changing from dolomite to argillite, respectively (Fig. 9). Karstic weathering and related evidence of exposure is not observed in cuttings or thin sections at the level of this boundary. However, the boundary is represented by a distinctive high-amplitude, continuous reflection in seismic profiles caused by the transition of lithotype from dolostone to argillite (Fig. 12 and Fig. 13).

Msb2 is an unconformity generated by subaerial exposure in the north-western part of the Tarim Basin; collapse breccia is present atop the boundary (Ye et al., 2014). This boundary records a marked and abrupt change in microfacies, and thereby interpreted depositional environments below and above. In Well Y1, the depositional environment changed from an evaporate tidal flat below, to a dolomite flat environment above (Fig. 8), with microfacies changing from gypsum dolomite to microcrystalline dolomite, respectively. The boundary can be traced basin-wide in seismic profiles, with moderate-amplitude reflections caused by the transition of lithotype from gypsum dolomite to crystalline dolomite (Fig. 13a-b).

Msb3 records a major transgressive surface developed in response to regional sea-level rise. In Well Y1, the inferred depositional environment changed from evaporate tidal flat below, to a marine restricted platform environment above (Liu et al., 2016), with microfacies changing from gypsum dolomite and argillaceous dolomite to finely crystalline dolomite, respectively (Fig. 8). In the seismic cross-sections, this boundary is represented by a high-amplitude, continuous reflection (Fig. 13a-b).

Within the major 2^{nd}-order sequences, eight superimposed 3^{rd}-order sequences (Sq1-Sq8) are recognized. Within these, six 3^{rd}-order sequence boundaries (Sb1, Sb2, Sb3, Sb4, Sb5 and Sb6) are identified in the study area. The 3^{rd}-order sequence boundaries record changes in depositional environments below and above as a result of sea-level fall and subsequent rise. The 2^{nd}-order sequence CS1 incorporates five nested 3rd -order sequences (Sq1, Sq2, Sq3, Sq4 and Sq5; Fig. 8-Fig. 10). The 2nd-order sequence CS2 incorporates three nested 3rd-order sequences (Sq6, Sq7 and Sq8; Fig. 8-Fig. 10).

4.4. Seismic facies and stratigraphic units

4.4.1. Seismic facies interpretation

In the 3D seismic volume of the carbonate platform in the Tarim Basin, eight seismic facies types (SMF1-SMF8) are identified based on different seismic reflection characteristics (internal reflection structure, continuity, amplitude and frequency) and external structure (Fig. 11).

4.4.2. Seismic stratigraphic units and depositional architecture

The Lower-Middle Cambrian strata are very thick (1000-1200 m) in the Tabei Uplift of the Tarim Basin. The evolution and distribution of depositional facies zones and their vertical and lateral variability (Yu et al., 2022; Zhang et al., 2015) remain unclear. Through the analysis of seismic reflection character, in combination with well-log data, cuttings and thin-section data from across the study area from the Tabei Uplift to the Manjiaer Depression, six stratigraphic units are identified in the studied Cambrian succession (Fig. 12 and Fig. 13). The spatiotemporal development of depositional facies under the isochronous framework in the Lower-Middle Cambrian has been mapped (Fig. 14 and

Fig. 15). Eight sequence boundaries, including three megasequence boundaries associated with the two 2nd-order sequences are identified in seismic profiles of the Lower-Middle Cambrian (Fig. 13a). Six carbonate progradational sediment bodies can be identified in the seismic profiles. Progradational bodies Pb1 and Pb2 are developed in Sq4 and Sq5, respectively. Progradational body Pb3 is developed in the TST of Sq6. Progradational bodies Pb4, Pb5 and Pb6 are developed in the HSTs of Sq6, Sq7 and Sq8, respectively. Progradational bodies Pb3-Pb6 of the Middle Cambrian are more aggradational and more progradational than Pb1-Pb2 of the Lower Cambrian.

Seismic Line 1 passes through wells Y1, Y2, and Y4 in the Tabei area, and extends northeast from the Tabei Uplift to the northern part of the Manjiaer depression (Fig. 1b). The two-way travel time (TWTT) of the Cambrian sedimentary succession near the Aman Slope in the west is from about 4.35s to about 5.05s, which is similar to the TWTT of 3.85s to 4.45s for that in the eastern Tabei Uplift. However, the TWTT of the Xiaoerbulake Formation decreases sharply to the east of Well Y3. The TWTT of the Middle Cambrian succession increases significantly to the east of Well Y3 and decreases sharply into the Manjiaer depression (Fig. 12).

Seismic Line 2 passes through wells Y1 and Y5, and extends eastward from the Tabei Uplift to the northern part of the Manjiaer depression (Fig. 1b). The thickness of Xiaoerbulake Formation decreases sharply from a maximum in well Y1 (TWTT from 4.82s to 5.05s) eastwards (Fig. 13a).

4.4.2.1 Second-order sequence CS1

Seismic stratigraphic units: The total thickness of the 2nd-order sequence CS1 in the west of the Tabei Uplift is greater than that in the east (Fig. 13). The 2nd-order sequence CS1 can be divided into four parts, corresponding to 3rd-order sequence- Sq1, Sq2, Sq3, Sq4 and Sq5. The lower part of CS1 (Sq1-Sq2) contains parallel, high-amplitude, continuous seismic reflections (SMF3) and is crossed by several wells. The middle two parts (Sq3 and Sq4) change from subparallel-parallel, moderate- to high-amplitude, moderately to highly continuous reflections (SMF1 and SMF2) in the west, to parallel, high-amplitude, continuous seismic reflections (SMF1) in the east. It crossed by wells Y1 and Y4, respectively. The upper part (Sq5) is characterized by subparallel, moderate amplitude, and moderate-high continuous reflections (SMF4 and SMF5) in the west. It is crossed by wells Y1 and Y2. The central and eastern parts are composed of mounded, chaotic, low continuous reflection and subparallel-moderate continuous reflections (SMF7), which transform eastward to parallel, high-amplitude, continuous seismic reflections (SMF8) (Fig. 13b).

Depositional architecture: In Sq1-Sq2, there was little variation in the lateral distribution of depositional facies. Vertically, Sq1 resulted in the accumulation of deep shelf facies (MA1) and is mainly composed of MF1 and MF2. The following Sq2 resulted in the accumulation of shallow shelf facies (MA2) and consisted mainly of MF3 and MF6. In Sq3, wells Y1, Y2 and Y3 in the west were located in the outer part of the middle ramp (MA4), consisting of MF4 and MF6. Horizontally, well Y4 in the east was located in the outer ramp (MA3), containing MF3. In Sq4, the depositional environment of the succession representing TST4 observed in each well was similar to that of TST3 in Sq3, while calcite content in Sq4 is reduced. The depositional environment in RST4 induced a vertical change from an outer middle ramp (MA4) setting to an inner middle ramp (MA5) and lagoon (MA6) setting. The MA5-MA6 is mainly composed of MF6-MF7. Well Y2 recorded shoal deposits (MA7) of a middle ramp setting, consisting of MF5 and MF13. In Sq5, the preserved thickness is greater in the east than in the west. In TST5, well Y2 was represented by mound-shoal complex (MA13) facies, containing MF14a and MF11 above the uppermost deposits of earlier RST4. In RST5, wells Y1 and Y2 recorded gypsum dolomite flat (MA9) and dolomite flat (MA8) deposits composed of MF8, MF9 and Mf15. Laterally, wells Y3 and Y4 began to develop platform margin shoal (MA14) deposits, consisting of MF10 and MF13. Generally, Sq5 preserved accumulations of two stages of platform-margin mound-shoal complexes (MA13) and one stage of platform margin shoal (MA14) deposit (Fig. 13c and Fig. 14).

4.4.2.2 Second-order sequence CS2

Seismic stratigraphic units: The thickness of CS2 increases sharply from well Y1 to well Y5 (Fig. 13a). Multiple progradational bodies, each with internal chaotic reflections, are identified in the platform margin (SMF6, SMF7) and crossed by wells Y4 and Y5. Subparallel, moderate amplitude, moderate-high continuous seismic reflections (seismic facies SMF4) are observed in the western platform. In addition, the deposits developed inside the platform margin shoals are characterized by subparallel-parallel, high amplitude, moderate-high continuous seismic reflection (SMF5; Fig. 13b).

Depositional architecture: In TST6 of Sq6, the depositional environment recorded in wells Y1 and Y2 changed from the gypsum dolomite flat (MA10) to dolomite flats (MA9), consisting of MF8 at the bottom and MF13 at the top. Laterally, wells Y3 and Y4 recorded development of a platform margin shoal (MA14). While well Y3 consisted of high-ennergy MF12 . well Y4 developed low-tomoderate-energy MF13 (Fig. 10). In RST6, the depositional environment recorded in wells Y1 and Y2 was gypsum-dolomite flat (MA10) composed of MF9 and MF15, whereas well Y3 changed to dolomite flat (MA11). Wells Y4 and Y5 recorded a mound-shoal complex (MA13) and platform margin shoal (MA14), consisting of MF14a, MF14b, MF12b and MF10, MF12a respectively. In TST7 of Sq7, wells Y1 and Y2 recorded gypsum-dolomite flat (MA10) and muddy dolomite flat (MA8), containing MF15 and MF9 respectively. Laterally, wells Y3 and Y4 recorded dolomite flat (MA9), and well Y5 recorded a transformation from a platform margin shoal (MA14) into a mound-shoal complex (MA13) composed of MF14a. In RST7, wells Y1 and Y2 recorded gypsum dolomite flat (MA10), consisting of MF9 and MF15. Laterally, wells Y3 and Y4 recorded dolomite flat (MA9) and intra-platform shoal (MA11), containing MF8 and MF13 respectively. Well Y5 recorded platform margin shoal (MA14) and mound-shoal complex (MA13). In TST8 of Sq8, the depositional environments recorded by successions in wells Y1, Y2 and Y3 remained similar. Well Y4 changed from an inner shoal (MA11) to an inner mound (MA12) composed of MF14a. Laterally, well Y5 recorded a change from a platform margin mound-shoal complex (MA14) to a dolomite flat (MA9) composed of MF8. In RST8, wells Y4 and Y5 recorded intercalated dolomite flat (MA9), inner shoal (MA11) and inner mound (MA12) deposits. Compared with Sq7, content of MF8 in Sq8 is increased. Generally, the platform margin zone developed four stages of mound-shoal complexes (MA13) and five stages of shoals (MA14) deposits (Fig. 13c and

Fig. 15).

4.5. Fischer plots and isotopes

4.5.1 Fischer plots

The Fischer plot was first proposed for the study of sea-level changes in cyclically arranged tidal-flat carbonate deposits (Fig. 16a). It was applied to explain the vertical stacking patterns of carbonate deposits and changes in accommodation with relative sea-level (Fischer, 1964). Previous studies have modified the original plotting method (Fig. 16b). However, the technique is not applicable in all conditions (Sadler et al., 1993). It is, however, suitable in cases where a shallow-water depositional environment has accumulated in response to accommodation generated via a steady rate of subsidence. Thick cycles generally record a long-term increase in accommodation space, whereby rapid relative sea-level rise was ongoing and uninterrupted. In contrast, thin cycles generally record a long-term decrease in accommodation, potentially caused by slow relative sea-level rise (cf. Goldhammer et al., 1990; Goldhammer et al., 1993). Therefore, the results of the Fischer-plot analysis can indicate change rate in relative sea-level.

The deposit cycles correlate with the scale factor of the Morlet wavelet function during the continuous wavelet transform, which can be used to analyze frequency characteristics of signals (Meyers et al., 1993). Generally, the recorded GR signals without uranium have a good response relationship to the identified microfacies (Fig. 8-Fig. 10). After performing continuous Morlet wavelet transform analysis on GR logging data, the wavelet coefficient curve which has notable cyclic properties can be obtained (Hu et al., 2018; Prokoph and Agterberg, 2000). Long-term surface exposure may result in missing records of high-frequency sea-level fluctuations in coastal areas (Goldhammer et al., 1990). However, through the observation of thin sections in the study area, no obvious candidate long-term exposure surfaces (Colombié and Strasser, 2005; Osleger and Read, 1991; Overstreet et al., 2003) were found in the interior of CS1 and CS2. By tracking specific points in the wavelet coefficient curves, the short-term periodic deposit cycles can be obtained. Based on the identified short-term high-frequency cycles, Fischer plots relating to data recovered from five wells are constructed (Fig. 8-Fig. 10 and 15; Guo et al., 2018a; Guo et al., 2018b; Wang et al., 2022; Yu et al., 2022).

The preserved depositional thickness of Sq1-Sq2 varies from 39 to 79.5 meters and the high-frequency cycles therein are on average only 0.5 meters thick (Fig. 8-Fig. 10). As such, these cycles are too thin to enable construction of a meaningful Fischer plot and to conduct continuous wavelet transform analysis. Therefore, analysis has been confined to the short-period, high-frequency cycles of Sq3-Sq5 in the Lower Cambrian (thickness max = 10.0 m; mean = 9.7 m; Min = 5.8 m), and to Sq6-Sq8 in the Middle Cambrian (thickness max = 14.2 m; mean = 9.5 m; min = 6.5 m). These high-frequency cycles correspond to the meter-scale cycles commonly about 10 m thick. Overall, well Y1 has the largest number of high-frequency cycles, well Y5 well has the least number of cycles, and well Y4 has the highest average thickness of cycles in Sq3-Sq8 (Table 2). Fischer plots have been constructed for these intervals, and six cycles can be identified on the cumulative deviation of average thickness in Sq3-Sq8 (Fig. 8-Fig. 10 and Fig. 16).

4.5.2 Carbon and oxygen isotopes

Previous studies have shown that the carbon isotope composition of marine carbonate rocks has a strong correlation with the production and burial of organic carbon (Stephens and Sumner, 2003). The generation and rapid burial of a large amount of organic carbon during major the episodes of global transgression period led to a decrease in ^{12}C and a relative increase in ^{13}C in seawater, resulting in a positive drift of $\delta^{13}C$ in marine carbonate rocks (Tissot, 1979). In contrast, the exposure of the continental shelf during episodes of major global regression will lead to the oxidation of a large amount of organic carbon, which will lead to cause an increase in ^{12}C and a relative decrease in ^{13}C in seawater, resulting in a relative decrease in $\delta^{13}C$ in marine carbonate rocks (Tissot, 1979). There is a negative correlation between $\delta^{13}C$ in carbonate rocks and global sea-level changes (Shembilu and Azmy, 2021), e.g. global sea level rise would be accompanied by a positive drift in $\delta^{13}C$. The C and O isotopes are analyzed in the wells Y1, Y2 and Y4, and eight cycles can be identified based on the C isotopes changes (Fig. 8-10).

In well Y1, the depth of Sq1-Sq2 ranges from 8781.5-8744 m, and $\delta^{13}C$ remained at a low value (Fig. 8). At the depth of 8744-8702 m, $\delta^{13}C$ began to drift positively from -1.9‰ to -0.2‰ (Fig. 8). In Sq3-Sq4, the thickness of most high-frequency cycles in the rising limb of the Fischer curve is greater than the average cycle thickness, and the corresponding $\delta^{13}C$ was drift to more positive values about 1.2‰ (Fig. 8). In the descending limb of the Fischer curve, the thin high-frequency cycles reflect a long-term decrease in accommodation space, and $\delta^{13}C$ began to drift negatively from 0.7‰ to -0.4‰ in the uppermost part of Sq4 (Fig. 8). In Sq5, from base to top, $\delta^{13}C$ first drifts negatively, and then drifted positively from -0.8‰ to 0.7‰. In Sq6-Sq8, the rising limb of the Fischer curve corresponds to a positive drift of $\delta^{13}C$, whereas the descending limb of the Fischer curve corresponds to a negative drifting of $\delta^{13}C$ (Fig. 8).

In well Y2, the variation of $\delta^{13}C$ is similar to well Y1 in the Sq1-Sq2. In Sq3-Sq4, the rising limb of the Fischer curve is associated with the sudden positive drift of $\delta^{13}C$ from -1.2‰ to 0.84‰ (Fig. 9). The upper part of the descending limb of the Fischer curve in the Sq4 sequence corresponds to a gradual negative drift from 0.46‰ to -0.75‰ and small-amplitude fluctuations of $\delta^{13}C$ (Fig. 9). In Sq5-Sq6, a large negative drift of $\delta^{13}C$ changed from 1.29‰ to -0.06‰ is evident (Fig. 9). In Sq7-Sq8, the characteristics of the Fischer curve is similar to those observed in Y1 well, with both positive and negative drift in carbon isotope values (Fig. 9).

In well Y4, $\delta^{13}C$ remained at a low value about -2.5‰ in Sq1-Sq2. In Sq3-Sq4, the thickness of Sq3-Sq4 is thin, and the rising limb of the Fischer curve corresponds to a gradual positive drift of $\delta^{13}C$ from -1.1‰ to 0.6‰, whereas the descending limb of the Fischer curve is associated with a significant negative drift of $\delta^{13}C$ from 0.6‰ to -0.3‰ (Fig. 10). In the rising limb of the Fischer curve in Sq5, $\delta^{13}C$ experienced fluctuations but an overall positive drift from -0.4‰ to 0.8‰, while the descending limb of the Fischer curve is associated with a gradual negative drift from 0.8‰ to -0.1‰ (Fig. 10). In Sq6-Sq8, the rising and descending limb of the Fischer curve corresponds to a gradual positive and negative drift of $\delta^{13}C$ respectively, while the rising and descending limb of the Fischer curve in Sq8 is associated with a sudden positive drift of $\delta^{13}C$ from 0.7‰ to 2‰ (Fig. 10).

5. Discussion

5.1. Sea-level changes

The paleo-water depth and RSL changes indicated by the microfacies and Fischer plot can be divided into eight cycles of sea-level rise and fall, consistent with global sea-level changes represented by the carbon isotopes (Fig. 8-10). For each of the eight cycles, reconstructed paleo-water depth changed from shallow, to deep, and back to shallow. The eight moderate-term sea-level cycles correspond to the 3rd-order sequences (Sq1-Sq8) and to the sequence units identified in the seismic sections (Fig. 13). The eight cycles of sea-level rise and fall can be divided into two overall long-term sea-level cycles that correspond to the 2nd-order sequences (CS1-CS2). The rising limbs of Fischer curves and the positive carbon isotope drifts correspond to the transgressive system tracts of the 3rd-order sequences. The descending limbs of Fischer curves and negative drifts correspond to the regressive system tracts.

During the CS1, the overall sea-level was high, and the RSL rose rapidly at first with the MFS present in Sq1 (Fig. 8-10). As RSL rapidly rose to the MFS, the microfacies were mostly dominated by MF1 and MF2 in Sq1-Sq2, indicating a deep-water environment. Then the RSL occurred a slow rise and regression in Sq3-Sq4, the paleo-water depth began to fall continuously, resulting in the disappearance of MF1 and the increase of MF5, MF7 and MF8 content. The depositional environment transformed from deep shelf to shallow ramp. Along with the RSL experienced regression in Sq5, the paleo-water depth reached the lowest, resulting in the appearance of MF13-MF15. The depositional environment is transformed into restricted platform and platform margin. During the CS2, the overall sea-level rose slowly; the MFS is present in Sq5 (Fig. 8-10). As RSL experienced a rapid and low-amplitude rose in Sq6, the paleo-water depth was deeper than Sq5, resulting in the short-term disappearance of MF15 and large-scale development of MF8, MF12 and MF13. The depositional environment became semi-restricted. Then the RSL occurred regression, the paleo-water depth began high-amplitude fall, resulting in the increase of MF15 content in the west and MF12-MF14 in the east. The restricted platform expanded broadly, and platform edge migrated eastward greatly. Overall, the RSL and paleo-water depth changes plays an important role in basin filling and sedimentary evolution.

5.2. Main factors controlling the evolution of carbonate platform

During the Cambrian, the Tarim Basin experienced an arid climate (Zhang et al., 2023). The basin was situated at a paleolatitude of between 30° north and south of the equator (Bai et al., 2017; Hoffman and Li, 2009). The water was warm and clear (cf. Schlager, 2003). These factors enabled the development of a major tropical shallow-water carbonate factory (Schlager, 2003). The interpreted paleo-wind direction changed from south-west to south-southwest in the Cambrian (Hu et al., 2023). The windward side had relatively high energy and developed microbial rocks (Berg and Pace, 2017; Michel et al., 2018), which were conducive to the formation of the rimmed platform. The high-angle of slope caused the carbonate deposits to accumulate in response to transport by waves, and enabled the formation of large-scale platform-margin mounds and shoals. Macro-reef building biological populations did not develop in the Cambrian, and microorganisms dominated by cyanobacteria played a leading role in the deposition and formation of carbonate rocks at the platform margin (Flügel, 2010; Pratt, 2009; Song et al., 2012). Moreover, water depth, hydrodynamic conditions and sediment types determined by RSL (relative sea-level) changes, controlled the morphology, internal structure and growth of the platform (Pomar, 2001). When water depth is below 60 m, microorganisms will probably multiply and are enabled to maintain high productivity (cf. Pomar and Haq, 2016), especially in the shallow and high-energy platform margin.

Paleo-water depth changes are controlled by regional tectonics, deposition rate and global sea-level changes (Vail, 1991). Deposition rate is relatively constant over the time of 3rd-order sequence and can be considered as a constant (Zhao, 2015). The biostratigraphy indicates that the Lower-Middle Cambrian was deposited in the Terreneuvian, Series 2 and Miaolingian (Chen et al., 2020). Comparison of the reconstructed paleo-water depth changes reported in this study with the global sea level curve (Haq and Schutter, 2008) and carbon isotopes curve, reveals that both contain six notable cycles of sea-level rise and fall – Sq3-Sq8 of this study (Fig. 17). This indicates that paleo-water depth changes reported here were consistent with models of global sea-level change. As such, global sea-level change was considered to be the main factor that controlled the structure and sedimentary evolution of the carbonate platform across this subsiding or passive margin that was subject to a relatively constant rate of basin subsidence (Bosence, 2005).

Overall, the development of the carbonate ramp in the Early Cambrian is attributed to the increase in carbonate production in the deep aphotic zone caused by the sea level decline (Huang et al., 2022). Whereas, the distal steepening feature in the eastern ramp is caused by the appearance of progradational bodies and the difference in subsidence rate between the Manjiaer Depression and the study area (Li et al., 2012). High-frequency sea level fluctuations will cause deposit to disperse and accumulated under deep water flat ramp, preventing forming high angle differential paleogeography (Williams et al., 2011). In the late Early Cambrian, as the sea level fall, the accommodation space decreased and the progradational bodies developed in the ramp setting. The progradational bodies continued to prograde from west to east and the difference in subsidence rate increased, resulting in a gradual increase in the angle of the ramp break. Due to the sea-level declined to the lowest value and its fluctuation range was small, making carbonate easy to deposit in situ (Williams et al., 2011). Affected by seawater waves and monsoons from the southwest to the west, the accumulation of moderate- to high-energy deposit increased the thickness and angle of the break, eventually forming a poorly rimmed carbonate platform.

In the Middle Cambrian, with the low-amplitude sea-level rise, the poorly rimmed carbonate platform margin has a greater production rate and continues to thicken to catch up with sea-level changes, causing a large amount of granular and microbial carbonate deposit. As deposits continued to accumulate, the paleogeography of the platform margin became higher, the slope angle became larger and the poorly rimmed carbonate platform transformed into a strongly rimmed carbonate platform. In addition, the obstruction of the platform margin and arid paleoclimate made the environment of intra-platform more restricted and the salinity of paleo-water increase. Since the high-salinity water environment is not conducive to the growth of microorganisms, microorganisms will accumulate at the platform margin near the open sea. Therefore, the platform margin has a higher carbonate production, making it more rimmed. As the accommodation space decrease caused by the continuous decline of sea-level, the platform margin prograde towards the basin, eventually forming a large-scale carbonate platform margin zone.

5.3. Platform development and evolution pattern

Since carbonate microfacies and platform types show great differences in time and space, establishing controls on depositional evolution is important (Gu et al., 2009; Pomar and Hallock, 2008). Previous studies have suggested that platform margin reef deposits could be observed, and weekly rimmed carbonate platforms developed in the late Early Cambrian in the Northern Tarim Basin (Gao and Fan, 2015; Pomar, 2001; Tucker, 1990; Wei et al., 2021).

The characteristics of depositional facies and sea-level changes indicate changes from relatively deep to shallow paleo-water, humid to arid climate, and open to restricted environmental settings. Based on the spatial and temporal distribution of depositional facies, the Lower-Middle Cambrian successions of Northern Tarim Basin are divided into four depositional types: broad shelf (Sq1-Sq2), distal steepening ramp (Sq3-Sq4), weekly rimmed platform (Sq5), and strongly rimmed platform (Sq6-Sq8). This study identifies platform types similar to those identified previously (Burchette and Wright, 1992; Tucker, 1990; Wilson, 1975) and builds upon these to explain the occurrence of depositional patterns (Fig. 18). The position of the identified depositional environments within the overall platform settings can be evaluated by analyzing the microfacies associations, paleo depositional profiles, and vertical and horizontal facies distribution (Noorian et al., 2021).

In the Lower Cambrian (Sq1-Sq5), the Tarim Basin was in a stable extensional tectonic background in the Early Caledonian (Liu et al., 2022). During Sq1-Sq2 period, along with substantial and rapid relative sea-level rise, broad deep shelf deposit developed, accompanied by syn-sedimentary faults and related siliceous hydrothermal activities (Fig. 18a). During Sq3-Sq4, regression occurred in RST3 (3) of Sq3 (3), with an increase in carbonate production in the deep aphotic zone and depositional pattern changing to the distal steepening ramp (Fig. 18b; Williamas et al., 2011; Huang et al., 2022). The distal steepening was caused by different subsidence rate between the Manjiaer Depression and this study area (Li et al., 2012). RSL fluctuations caused sediments to disperse and are difficult to form under regional high paleogeography, such as in deep ramps (Williams et al., 2011). During Sq5 period, regression reached maximum extent in CS1 and the accumulation of moderate- to high-energy mound and shoal deposits developed along the slope (Gao and Fan, 2015; He et al., 2017), forming a weekly rimmed carbonate platform. Semi-restricted platform developed due to the blocking effect of margin mounds and shoal deposits (Fig. 18c).

In the Middle Cambrian (Sq6-Sq8), the Tarim Basin was dominated by strongly rimmed platform deposits. During TST5 of Sq6, a short-term period of rapid sea-level rise ensued; in response, the depositional environment in the western platform changed into the restricted-open platform. Due to the high carbonate production, deposits continued to thicken to catch up with relative sea-level changes in the platform margin (Huang et al., 2022), and a strongly rimmed carbonate platform developed (Fig. 19a). During RST5 to RST7, a long-term period of slow relative sea-level rise ensured and accommodation gradually decreased in response to ongoing sedimentation, the platform margin continued to prograde towards the basin, forming the large-scale platform margin zone. Due to the barrier of platform margin and the arid paleo-climate, salinity of paleo-water increased in the western platform which evolved into a restricted platform (Fig. 19b).

6. Conclusions

Based on the depositional facies, the sequence architecture and relative sea-level changes using well and core data for petrographic observations, geochemical data analyses, Fischer curves construction and integration with 3D seismic interpretation of the Lower-Middle Cambrian in the Tabei Uplift of the Tarim Basin, the following conclusions can be drawn.

1. From analysis of sixteen microfacies (MF1–MF16) and fourteen microfacies associations (MA1-MA14), fourteen depositional facies are recognized in the Lower-Middle Cambrian in the Northern Tarim Basin: deep and shallow shelf, outer ramp, inner middle ramp, outer middle ramp, lagoon and shoal of middle ramp, muddy dolomite flat, gypsum dolomite flat of restricted platform, dolomite flat, inner shoal and inner mound of open platform, and mound-shoal complex and shoal of platform margin. The carbonate depositional environment evolved from a shelf (Sq1-Sq2), to a distal steepening ramp (Sq3-Sq4), to a weekly rimmed platform (Sq5), and finally to a strongly

rimmed platform (Sq6-Sq8). A shelf, ramp and rimmed platform carbonate depositional pattern has been established and six stages of progradational rimmed platform margin deposits composed by mound-shoal complexes and shoals have been characterized.

2. The Lower-Middle Cambrian in the study area can be classified into two 2^{nd}-order stratigraphic sequences (CS1 and CS2) within which eight 3^{rd}-order sequences are superimposed. Within most of the 3^{rd}-order sequences, transgressive and regressive system tracts are identified. Paleo-water depth and relative sea-level changes were reconstructed using microfacies characteristics and Fischer plots based on the continuous wavelet transform of gamma-ray wireline logging data, respectively. Paleo-water depth inferred from the microfacies are highly consistent with the global sea-level change indicated by the carbon isotopes. Reconstructed Paleo-water depth changes can be divided into eight episodes of rise and fall corresponding to the eight 3^{rd}-order sequences, Sq1-Sq8. A long-term, major maximum flooding surface occurs at the end of the transgressive system tract of Sq1.

3. The existence of favorable prevailing paleocurrents (including paleowinds) and the development of a slope break zone enabled the development of the carbonate platform in the northern Tarim Basin during the Cambrian. Evolution of the depositional system was primarily controlled by tectonics and global sea-level changes. The comparison of paleo-water depth with the global sea-level change curve demonstrates that the ongoing rate of tectonic subsidence in the study area during the deposition of the Lower-Middle Cambrian was relatively constant; global sea-level change was the main factor controlling rimmed platform architecture.

4. To date, Ediacrian-Cambrian rimmed carbonate platforms have been poorly documented. Hence, this study provides valuable information regarding the composition and architecture of a Cambrian rimmed carbonate platform. As well as documenting the nature of this platform, this study may act as an analogue to help inform the characteristics of other, less well preserved Ediacrian-Cambrian rimmed carbonate platforms.

Author contribution statement

Author contributions: Qing He: Conceptualization, writing-original draft, writing-review & editing, methodology, investigation, funding acquisition; Kaibo Shi: writing-review & editing, validation, resources; Yongsheng Ma, writing-review & editing, validation; Bo Liu: project administration, writing-review & editing, supervision, resources; Jun Han: writing-review & editing, resources; Jun Li: data curation; Xiangyu Bai: data curation; Chun Wu: writing-review & editing; Adam D. McArthur: writing-review & editing, validation; Nigel P. Mountney: writing-review & editing, validation.

Declaration of competing interest

The authors declare that they have no known competing financial interests or personal relationships that could have appeared to influence the work reported in this paper.

Acknowledgments

This research was supported by the Science and Technology Major Project of Northwest Exploration and Production Company of SINOPEC. Number: KY2022-034. Thanks to Associate Prof. Jinyou He (China University of Geosciences, Beijing) for the discussion on structure and content of the essay. We would also like to thank Dr. Jinxin Yu (CNOOC) and Dr. Jiangwei Ming (CNODC) for the discussion on facies analysis. We would like to express our deep thanks and gratitude to all editorial staff.

References

Bai, Y., Luo, P., Wang, S., Zhou, C., Zhai, X., Wang, S., Yang, Z., 2017. Structure characteristics and major controlling factors of platform margin microbial reef reservoirs: A case study of Xiaoerbulak Formation, Lower Cambrian, Aksu area, Tarim Basin, NW China. Petrol. Explor. Dev. 44, 349-358.

Bai, Y., Xu, A., Liu, W., Zhao, Z., Luo, P., 2019. Sedimentary characteristics of Lower and Middle Cambrian diamict in the northwestern Tarim Basin. Nat. Gas. Ind. 39, 46-57.

Beauchamp, B., Grasby, S.E., 2012. Permian lysocline shoaling and ocean acidification along NW Pangea led to carbonate eradication and chert expansion. Palaeogeogr. Palaeoclimatol. Palaeoecol. 350, 73-90.

Bosence, D., Cross, N., Hardy, S., 1998. Architecture and depositional sequences of tertiary fault-block carbonate platforms; an analysis from outcrop (Miocene, Gulf of Suez) and computer modelling. Marine and Petroleum Geology 15, 203-221.

Berg, P., Pace, M.L., 2017. Continuous measurement of air-water gas exchange by underwater eddy covariance. Biogeosciences 14, 5595-5606.

Bosence, D., 2005. A genetic classification of carbonate platforms based on their basinal and tectonic settings in the Cenozoic. Sed. Geol. 175, 49-72.

Bosence, D.W.J., Wood, J.L., Rose, E.P.F., Qing, H., 2000. Low- and high-frequency sea-level changes control peritidal carbonate cycles, facies and dolomitization in the Rock of Gibraltar (Early Jurassic, Iberian Peninsula). J. Geol. Soc. London. 157, 61-74.

Burchette, T.P., Wright, V.P., 1992. Carbonate ramp depositional systems. Sed. Geol. 79, 3-57.

Cao, Y., Li, H., Yan, L., Wang, H., Zhang, J., Yang, M., Zhao, Y., 2018. The sectional evolution characteristics of Cambrian platform margin in Manxi area of Tarim Basin and its differences in source-reservoir-cap combination conditions. Nat. Gas. Geosci. 29, 796-806.

Castro, J.M., de Gea, G.A., Ruiz-Ortiz, P.A., Nieto, L.M., 2008. Development of carbonate platforms on an extensional (rifted) margin: the Valanginian–Albian record of the Prebetic of Alicante (SE Spain). Cretac. Res. 29, 848-860.

Catuneanu, O., 2019. Model-independent sequence stratigraphy. Earth-Science Reviews 188, 312-388.

Catuneanu, O., Abreu, V., Bhattacharya, J., Blum, M.D., Dalrymple, R.W., Eriksson, P.G., Fielding, C.R., Fisher, W.L., Galloway, W.E., Gibling, M.R., Giles, K.A., Holbrook, J., Jordan, R., Kendall, C.G.S.C., Macurda, B., Martinsen, O.J., Miall, A.D., Neal, J.E., Nummedal, D., Pomar, L., Posamentier, H.W., Pratt, B.R., Sarg, J.F., Shanley, K.W., Steel, R.J., Strasser, A., Tucker, M.E., Winker, C.D., 2009. Towards the standardization of sequence stratigraphy. Earth-Sci. Rev. 92, 1-33.

Catuneanu, O., Khalifa, M.A., Wanas, H.A., 2006. Sequence stratigraphy of the Lower Cenomanian Bahariya Formation, Bahariya Oasis, Western Desert, Egypt. Sed. Geol. 190, 121-137.

Chen, D., Tucker, M.E., Zhu, J., Jiang, M., 2001. Carbonate sedimentation in a starved pull-apart basin, Middle to Late Devonian, southern Guilin, South China. Basin Res. 13, 141-167.

Chen, Q., Chu, C., Yang, X., Hu, G., Shi, Z., Jiang, H., Shen, B., Liu, W., 2015a. Sedimentary model and development of the Cambrian source rocks in the Tarim Basin, NW China. Petrol. Geol. Exper. 37, 689-695.

Chen, Q., Yang, X., Chu, C., Hu, G., Shi, Z., Jiang, H., Liu, W., 2015b. Recognition of depositional environment of Cambrian source rocks in Tarim Basin. Oil Gas Geol. 36, 880-887.

Chen, X., Xu, Q., Hao, F., Chen, Y., Yi, Y., Hu, F., Wang, X., Tian, J., Wang, G., 2023. Dolomite reservoir formation and diagenesis evolution of the Upper Ediacaran Qigebrak Formation in the Tabei area,Tarim Basin. Sci. China-Earth Sci. 66, 2311-2331.

Chen Y, Zhang Y, Wu Y, Zhou P, Li K, Wang X., 2020. Discovery of SPICE and carbon isotope stratigraphic correlation of the Cambrian Furongian Series in Tarim Craton, NW China. Science China Earth Sciences, 63: 1330–1338.

Cloyd, K.C., Demicco, R.V., Spencer, R.J., 1990. Tidal Channel, Levee, and Crevasse-Splay Deposits from a Cambrian Tidal Channel System: A New Mechanism to Produce Shallowing-Upward Sequences. J. Sediment. Petrol. 60, 73-83.

Colombié, C., Strasser, A., 2005. Facies, cycles, and controls on the evolution of a keep-up carbonate platform (Kimmeridgian, Swiss Jura). Sedimentology 52, 1207-1227.

Daidu, F., Yuan, W., Min, L., 2013. Classifications, sedimentary features and facies associations of tidal flats. J. Palaeogeogr. 2, 66-80.

Diedrich, C., 2002. Vertebrate track bed stratigraphy at new megatrack sites in the Upper Wellenkalk Member and orbicularis Member (Muschelkalk, Middle Triassic) in carbonate tidal flat environments of the western Germanic Basin. Paleogeogr. Paleoclimatol. Paleoecol. 183, 185-208.

Dunham, R.J., 1962. Classification of carbonate rocks according to depositional textures. In: Ham, W.E., (Ed.), Classification of Carbonate Rocks. AAPG Memoir, vol. 1, pp. 108–121.

Elrick, M., Read, F.J., 1991. Cyclic ramp-to-basin carbonate deposits, lower Mississippian, Wyoming and Montana: a combined field and computer modeling study. J. Sediment. Petrol. 61 (7), 1194–1224.

Embry, A.F., 1993. Transgressive–regressive (T–R) sequence analysis of the Jurassic succession of the Sverdrup Basin, Canadian Arctic Archipelago. Can. J. Earth Sci. 30, 301-320.

Feng, Z., Bao, Z., Wu, M., Jin, Z., Shi, X., 2006. Lithofacies palaeogeography of the Cambrian in Tarim area. J. Palaeogeogr. 8, 427-439.

Fischer, A.G., 1964. The Lofer cyclothems of the alpine Triassic. In: Merriam, D.F., (Ed.), Symposium on Cyclic Sedimentation. Kansas Geological Survey, Bulletin, vol. 169, pp. 107–148.

Flügel, E., 2010. Microfacies of Carbonate Rocks, Analysis, Interpretation and Application. Springer Berlin, Heidelberg.

Gao, Z., Ding, Q., Hu, X., 2015. Characteristics and controlling factors of carbonate intra-platform shoals in the Tarim Basin, NW China. J. Pet. Sci. Eng. 127, 20-34.

Gao, Z., Fan, T., 2015. Carbonate platform-margin architecture and its influence on Cambrian-Ordovician reef-shoal development, Tarim Basin, NW China. Mar. Pet. Geol. 68, 291-306.

Gao, Z., Shi, J., Lv, J., Chang, Z., 2022. High-frequency sequences, geochemical characteristics, formations, and distribution predictions of the lower Cambrian Yuertusi Formation in the Tarim Basin. Mar. Pet. Geol.146, 105966.

Ge, R., Zhu, W., Wilde, S.A., He, J., Cui, X., Wang, X., Zheng, B., 2014. Neoproterozoic to Paleozoic long-lived accretionary orogeny in the northern Tarim Craton. Tectonics. 33, 302-329.

Geyman, E.C., Maloof, A.C., Dyer, B., 2021. How is sea level change encoded in carbonate stratigraphy? Earth Planet Sci. Lett. 560, 116790.

Gil, J., Garcia-Hidalgo, J.F., Segura, M., Garcia, A., Carenas, B., 2006. Stratigraphic architecture, palaeogeography and sea-level changes of a third order depositional sequence: The late Turonian-early Coniacian in the northern Iberian Ranges and Central System (Spain). Sed. Geol. 191, 191-225.

Goldhammer, R.K., Dunn, P.A., Hardie, L.A., 1990. Depositional cycles, composite sea-level changes, cycle stacking patterns, and the hierarchy of stratigraphic forcing: Examples from Alpine Triassic platform carbonates. Geol. Soc. Am. Bull. 102, 535-562.

Goldhammer, R.K., Lehmann, P.J., Dunn, P.A., 1993. The origin of high-frequency platform carbonate cycles and third-order sequences (Lower Ordovician El Paso Gp, West Texas); constraints from outcrop data and stratigraphic modeling. J. Sediment. Res. 63, 318-359.

Graziano, R., 2000. The Aptian–Albian of the Apulia Carbonate Platform (Gargano Promontory, southern Italy): evidence of palaeoceanographic and tectonic controls on the stratigraphic architecture of the platform margin. Cretac. Res. 21, 107-126.

Gu, J., Ma, F., Ji, L., 2009. Types, characteristics and main controlling factors of carbonate platform. J. Palaegeogr. 11, 21-27.

Guan, S., Zhang, C., Ren, R., Zhang, S., Wu, L., Wang, L., Ma, P., Han, C., 2019. Early Cambrian syndepositional structure of the northern Tarim Basin and a discussion of Cambrian subsalt and deep exploration. Petrol. Explor. Dev. 46, 1075-1086.

Guo, C., Chen, D., Song, Y., Zhou, X., Ding, Y., Zhang, G., 2018a. Depositional environments and cyclicity of the Early Ordovician carbonate ramp in the western Tarim Basin (NW China). J. Asian Earth Sci. 158, 29-48.

Guo, C., Chen, D., Zhou, X., Ding, Y., Wei, W., Zhang, G., 2018b. Depositional facies and cyclic patterns in a subtidal-dominated ramp during the Early-Middle Ordovician in the western Tarim Basin (NW China). Facies 64.

Haq, B.U., Schutter, S.R., 2008. A chronology of Paleozoic sea-level changes. Science 322, 64-68.

He, B., Jiao, C., Xu, Z., Cai, Z., Zhang, J., Liu, S., Li, H., Chen, W., Yu, Z., 2016. The paleotectonic and paleogeography reconstructions of the Tarim Basin and its adjacent areas (NW China) during the late Early and Middle Paleozoic. Gondwana Research 30, 191-206.

He, F., Lin, C., Liu, J., Zhang, Z., Zhang, J., Yan, B., Qu, T., 2017. Migration of the Cambrian and Middle-Lower Ordovician carbonate platform margin and its relation to relative sea level changes in southeastern Tarim Basin. Oil Gas Geol. 38, 711-721.

Heldt, M., Lehmann, J., Bachmann, M., Negra, H., Kuss, J., 2010. Increased terrigenous influx but no drowning: palaeoenvironmental evolution of the Tunisian carbonate platform margin during the Late Aptian. Sedimentology 57, 695-719.

Herrmann, A.D., Gordon, G.W., Anbar, A.D., 2018. Uranium isotope variations in a dolomitized Jurassic carbonate platform (Tithonian; Franconian Alb, Southern Germany). Chem. Geol. 497, 41-53.

Hoffman, P.F., Li, Z.-X., 2009. A palaeogeographic context for Neoproterozoic glaciation. Palaeogeogr.

Palaeoclimatol. Palaeoecol. 277, 158-172.

Hsu, K.J., Siegenth.C, 1969. Preliminary experiments on hydrodynamic movement induced by evaporation and their bearing on the dolomite problem. Sedimentology 12, 11-25.

Hu, C., Han, C., Ma, J., Wang, W., Zhao, F., Sun, W., 2023. Reconstruction of paleowind directions during the Cambrian-Ordovician in the Tarim Basin, Northwestern China. Palaeogeogr. Palaeoclimatol. Palaeoecol. 609. 111316.

Hu, M., Sun, C., Gao, D., 2019. Characteristics of tectonic-lithofacies paleogeography in the Lower Cambrian Xiaoerbulake Formation,Tarim Basin. Oil Gas Geol. 40, 12-23.

Hu, X., Fan, T., Gao, Z., Wu, P., 2018. Fischer Plot and Its Response to the Changes of the Early Ordovician Sea in the Bachu Area,Tarim Basin. Geol. Sci. Technol. Inf. 37, 88-95.

Huang, B., Xu, B., Zhang, C., Li, Y.a., Zhu, R., 2005. Paleomagnetism of the Baiyisi volcanic rocks (ca. 740Ma) of Tarim, Northwest China: A continental fragment of Neoproterozoic Western Australia? Precambr. Res. 142, 83-92.

Huang, S., Tong, H., Liu, L., Hu, Z., Zhang, X., Huan, J., Huang, K., 2009. Petrography, geochemistry and dolomilization mechanisms of Feixianguan dolomites in Triassic, NE Sichuan, China. Acta Petrol. Sin. 25, 2363-2372.

Huang, Y., Duan, T., Fan, T., Liu, Y., Shen, L., Zhang, W., Li, M., Zhang, D., 2022. Depositional evolution history and formation mechanism of Cambrian carbonate platforms in Tahe area: insights from stratigraphic forward modelling. Acta Petrol. Sin. 43, 617-636.

Huang, Y., Fan, T., Berra, F., 2020. Architecture and paleogeography of the Early Paleozoic carbonate systems in the east-central Tarim Basin (China): Constraints from seismic and well data. Mar. Pet. Geol. 113, 104147.

James, N.P., Vonderborch, C., 1991. Carbonate shelf edge off southern Australia: A prograding open-platform margin. Geology 19, 1005-1008.

Jia, C., 1999. Structural characteristic and oil/gas accumulative regularity in Tarim Basin. Xinjiang Petrol. Geol. 20, 177-183.

Jiang, W., Gao, Z., Hu, Z., Zhao, Y., Chu, C., 2021a. Sedimentary Filling Evolution and Hydrocarbon Control of High Frequency Sequence in Yurtus Formation, Tarim Basin. Geoscience 35, 349-364.

Jiang, W., Luo, Q., Shi, K., Liu, B., Wang, Y., Gao, X., 2021b. Origin of a microbial-dominated carbonate reservoir in the Lower Cambrian Xiaoerbulake Formation, Bachu-Tazhong area, Tarim Basin, NW China. Mar. Pet. Geol. 133.

Lai, J., Bao, M., Liu, S., Li, D., Wang, S., Yang, K., Chen, X., Wang, G., Ding, X., 2021. Prediction of high quality deep and ultra-deep dolostones reservoirs in Tarim Basin by well logs. J. Palaegeogra. 23, 1225-1242.

Li, J., Jiao, C., Wang, X., Zhang, Z., 2012. The tectonic evolution of Cambrian in Tarim Basin. Chinese Geol. Sin. 47, 575-587.

Li, Z.-X., Evans, D.A.D., Halverson, G.P., 2013. Neoproterozoic glaciations in a revised global palaeogeography from the breakup of Rodinia to the assembly of Gondwanaland. Sed. Geol. 294, 219-232.

Lin, C., Li, S., Liu, J., Qian, Y., Luo, H., Chen, J., Peng, L., Rui, Z., 2011. Tectonic framework and paleogeographic evolution of the Tarim basin during the Paleozoic major evolutionary stages. Acta Petrol. Sin. 27, 210-218.

Lin, C., Yang, H., Liu, J., Cai, Z., Peng, l., Yang, X., Yang, Y., 2008. Paleohigh geomorphology and paleogeographic framework and their controls on the formation and distribution of stratigraphic traps in the Tarim Basin. Oil Gas Geol. 29, 189-197.

Liu, C., Li, G., Luo, P., Wang, M., Luo, M., Liu, Y., 2016. Seismic Sequences, Evolution and Control Factors of Large Cambrian Progradational Platform-Slope System in the Northern Tarim Basin, Northwest China. Acta Geol. Sin. 90, 669-687.

Liu, Y., Hu, M., Zhang, S., 2022. Types, structural evolution difference and petroleum geological significance of Cambrian-Ordovician carbonate platforms in Gucheng-Xiaotang area, Tarim Basin, NW China. Petrol. Explor. Dev. 49, 1019-1032.

Liu, Z., Deng, K., Shi, Z., Tian, Y., Wang, Y., Shen, F., Tan, Q., Gong, X., 2020. Sedimentary facies and model of shallow water carbonates platform of the Lower Cambrian Longwangmiao Formation in Sichuan Basin. J. Palaegeogra. 22, 504-522.

Longhitano, S.G., Mellere, D., Steel, R.J., Ainsworth, R.B., 2012. Tidal depositional systems in the rock record: A review and new insights. Sed. Geol. 279, 2-22.

Markello, J.R., Koepnick, R.B., Waite, L.E., Collins, J.F., 2008. The Carbonate Analogs Through Time (Catt) Hypothesis and the Global Atlas of Carbonate Fields—A Systematic and Predictive Look at Phanerozoic Carbonate Systems, in: Lukasik, J., Simo, J.A. (Eds.), Controls on Carbonate Platform and Reef Development. SEPM Society for Sedimentary Geology, p. 0.

Meyers, S.D., Kelly, B.G., O'Brien, J.J., 1993. An Introduction to Wavelet Analysis in Oceanography and Meteorology: With Application to the Dispersion of Yanai Waves. Mon. Weather Rev. 121, 2858-2866.

Michel, J., Borgomano, J., Reijmer, J.J.G., 2018. Heterozoan carbonates: When, where and why? A synthesis on parameters controlling carbonate production and occurrences. Earth-Sci. Rev. 182, 50-67.

Montanez, I.P., Read, J.F., 1992. Eustatic control on early dolomitization of cyclic peritidal carbonates: Evidence from the Early Ordovician Upper Knox Group, Appalachians. Geol. Soc. Am. Bull. 104, 872-886.

Naderi-Khujin, M., Tavakoli, V., Seyrafian, A., Vaziri-Moghaddam, H., 2020. How a mud-dominated ramp changed to a carbonate–clastic oil reservoir: Sea-level fluctuations in cretaceous of the central Persian Gulf. Mar. Petrol. Geol. 116, 104301.

Ni, X., Shen, A., Chen, Y., Guan, B., Yu, G., Yan, W., Xiong, R., Li, W., Huang, L., 2015. Cambrian Carbonate Platform Types,Platform Margin Segmentation Characteristics and Exploration Enlightenment in Tarim Basin. Nat. Gas Geosci. 26, 1245-1255.

Noorian, Y., Moussavi-Harami, R., Hollis, C., Reijmer, J.J.G., Mahboubi, A., Omidpour, A., 2022. Control of climate, sea-level fluctuations and tectonics on the pervasive dolomitization and porosity evolution of the Oligo-Miocene Asmari Formation (Dezful Embayment, SW Iran). Sed. Geol. 427, 106048.

Noorian, Y., Moussavi-Harami, R., Reijmer, J.J.G., Mahboubi, A., Kadkhodaie, A., Omidpour, A., 2021. Paleo-facies distribution and sequence stratigraphic architecture of the Oligo-Miocene Asmari carbonate platform (southeast Dezful Embayment, Zagros Basin, SW Iran). Mar. Petrol. Geol. 128, 105016.

Osleger, D., 1991. Subtidal carbonate cycles: implications for allocyclic vs. autocyclic controls. Geology 19, 917–920.

Osleger, D., Read, J.F., 1991. Relation of eustasy to stacking patterns of meter-scale carbonate cycles, Late Cambrian, U.S.A. J. Sed. Petrol. 61, 1225-1252.

Overstreet, R.B., Oboh-Ikuenobe, F.E., Gregg, J.M., 2003. Sequence stratigraphy and depositional facies of Lower Ordovician cyclic carbonate rocks, southern Missouri, USA. J. Sed. Res. 73, 421-433.

Phelps, R.M., Kerans, C., Loucks, R.G., Da Gama, R.O.B.P., Jeremiah, J., Hull, D., 2014. Oceanographic and eustatic control of carbonate platform evolution and sequence stratigraphy on the Cretaceous (Valanginian-Campanian) passive margin, northern Gulf of Mexico. Sedimentology 61, 461-496.

Pomar, L., 2001. Types of carbonate platforms: a genetic approach. Basin Res. 13, 313-334.

Pomar, L., Aurell, M., Bádenas, B., Morsilli, M., Al- Awwad, S.F., 2015. Depositional model for a prograding oolitic wedge, Upper Jurassic, Iberian basin. Mar. Petrol. Geol. 67, 556-582.

Pomar, L., Brandano, M., Westphal, H., 2004. Environmental factors influencing skeletal grain sediment associations: a critical review of Miocene examples from the western Mediterranean. Sedimentology 51, 627-651.

Pomar, L., Hallock, P., 2008. Carbonate factories: A conundrum in sedimentary geology. Earth-Sci. Rev. 87, 134-169.

Pomar, L., Haq, B.U., 2016. Decoding depositional sequences in carbonate systems: Concepts vs experience. Glob. Planet. Chang. 146, 190-225.

Prokoph, A., Agterberg, F.P., 2000. Wavelet analysis of well-logging data from oil source rock, Egret Member, offshore eastern Canada. AAPG Bull. 84, 1617-1632.

Ren, J., Song, J., Liu, S., Zhao, R., Luo, Z., Li, Z., Jin, X., Ma, X., Li, K., Ye, Y., Ding, Y., Li, W., Zhao, L., Tian, L., 2023. Framework and sedimentary model of microbial mound-bank complex in Member 2 of Dengying Formation,Sichuan Basin. Acta Petrol. Sin. 44, 312-328.

Rosenau, N.A., Herrmann, A.D., Leslie, S.A., 2012. Conodont apatite δ18O values from a platform margin setting, Oklahoma, USA: Implications for initiation of Late Ordovician icehouse conditions. Paleogeogr. Paleoclimatol. Paleoecol. 315, 172-180.

Sadler, P.M., Osleger, D.A., Montanez, I.P., 1993. On the Labeling, Length, and Objective Basis of Fischer Plots. J. Sed. Petrol. 63, 360-368.

Santantonio, M., Scrocca, D., Lipparini, L., 2013. The Ombrina-Rospo Plateau (Apulian Platform): Evolution of a Carbonate Platform and its Margins during the Jurassic and Cretaceous. Mar. Petrol. Geol. 42, 4-29.

Schlager, W., 2003. Benthic carbonate factories of the Phanerozoic. Int. J. Earth Sci. 92, 445-464.

Scholle, P.A., Ulmer-Scholle, D.S., 2003. A color guide to the petrography of carbonate rocks: grains, textures, porosity, diagenesis, 77. AAPG Memoir, pp. 1–486.

Scott, R.W., Simo, J.A.T., Scott, R.W., Masse, J.-P., 1993. Cretaceous Carbonate Platform, U.S. Gulf Coast. In: Simo, T.J.A., Scott, R.W., Masse, J.-P. (Eds.), Cretaceous Carbonate Platforms, AAPG Memoir 56, pp. 97-109.

Servais, T., Cascales-Miñana, B., Harper, D.A.T., Lefebvre, B., Van Bocxlaer, B., Wang, W., 2023. Cambrian explosion and Ordovician biodiversification or Cambrian biodiversification and Ordovician explosion? Evolving Earth 1, 100018.

Shang, Y., Gao, Z., Fan, T., Wei, D., Wang, Z., Karubandika, G.M., 2020. The Ediacaran–Cambrian boundary in the Tarim Basin, NW China: Geological data anomalies and reservoir implication. Marine and Petroleum Geology 111, 557-575.

Shembilu, N., Azmy, K., 2021. Carbon-isotope stratigraphy of the Middle-Upper Cambrian in eastern Laurentia: Implications for global correlation. Mar. Petrol. Geol. 128, 105052.

Shi, K., Liu, B., Jiang, W., Luo, Q., Gao, X., 2018. Nanhua-Sinian tectono-sedimentary framework of Tarim Basin,NW China. Oil Gas Geol. 39, 862-877.

Song, J., Luo P., Yang S., Zhai X., Zhou G., Lu P., 2012. Carbonate rock microbial construction of the

Lower Cambrian Xiaoerblak Formation in Sugaitblak area, Tarim Basin. J. Palaeogeogra. 14, 341-254.
Stephens, N.P., Sumner, D.Y., 2003. Late devonian carbon isotope stratigraphy and sea level fluctuations, Canning Basin, Western Australia. Paleogeogr. Paleoclimatol. Paleoecol. 191, 203-219.
Tan, L., Liu, H., Chen, K., Ni, H., Zhou, G., Zhang, X., Yan, W., Zhong, Y., Lyu, W., Tan, X., Zhang, K., 2022. Sequence sedimentary evolution and reservoir distribution in the third and fourth members of Sinian Dengying Formation, Gaomo area, Sichuan Basin, SW China. Petrol. Explor. Dev. 49, 1004-1018.
Tissot, B., 1979. Effects on prolific petroleum source rocks and major coal deposits caused by sea-level changes. Nature 277, 463-465.
Tucker, M.E.W., V. Paul, 1990. Carbonate Sedimentology. Blackwell Scientific Publication, Oxford, pp. 482.
Vail, P.R., 1991. The stratigraphic signatures of tectonics, eustacy and sedimentology - an overview. Cycles and Events in Stratigraphy, 11(3), 617–659.
Wagner, T., Sinninghe Damsté, J.S., Hofmann, P., Beckmann, B., 2004. Euxinia and primary production in Late Cretaceous eastern equatorial Atlantic surface waters fostered orbitally driven formation of marine black shales. Paleoceanography 19. PA3009.
Wang, E., Li, M., Ma, X., Qian, M., Cao, T., Li, Z., Yang, W., Jin, Z., 2024. Diahopane and diasterane as the proxies for paleoenvironment, hydrocarbon generation condition, and shale oil accumulation. Chemical Geology 670, 122447.
Wang, E., Fu, Y., Guo, T., Li, M., 2025. A new approach for predicting oil mobilities and unveiling their controlling factors in a lacustrine shale system: Insights from interpretable machine learning model. Fuel 379, 132958.
Wang, Q., Liu, J., Lin, C., Li, H., 2022. Depositional evolution, sequence stratigraphic framework and its response to relative sea-level change, the Middle and Lower Ordovician carbonate system on outcrops, north-western margin of Tarim Basin. Mar. Petrol. Geol. 146. 105909.
Wang, X., Li, B., Yang, X., Wen, L., Xu, L., Xie, S., Du, Y., Feng, M., Yang, X., Wang, Y., Pei, S., 2021. Characteristics of Guangyuan-Wangcang trough during late Middle Permian and its petroleum geological significance in northern Sichuan Basin, SW China. Petrol. Explor. Dev. 48, 562-574.
Wei, G., Zhu, Y., Zheng, J., Yu, G., Ni, X., Yan, L., Tian, L., Huang, L., 2021. Tectonic-lithofacies paleogeography,large-scale source-reservoir distribution and exploration zones of Cambrian subsalt formation,Tarim Basin,NW China. Petrol. Explor. Dev. 48, 1114-1126.
Williams, H.D., Burgess, P.M., Wright, V.P., Della Porta, G., Granjeon, D., 2011. Investigating Carbonate Platform Types: Multiple Controls and a Continuum of Geometries. J. Sed. Res. 81, 18-37.
Wilson, J.L., 1975. Carbonate Facies in Geologic History. Springer-Verlag, New York, pp. 1–471.
Wood, R., Liu, A.G., Bowyer, F., Wilby, P.R., Dunn, F.S., Kenchington, C.G., Cuthill, J.F.H., Mitchell, E.G., Penny, A., 2019. Integrated records of environmental change and evolution challenge the Cambrian Explosion. Nat. Ecol. Evol. 3, 528-538.
Wright, V.P., Burgess, P.M., 2005. The carbonate factory continuum, facies mosaics and microfacies: an appraisal of some of the key concepts underpinning carbonate sedimentology. Facies 51, 17-23.
Xi, S., Xiong, Y., Liu, X., Lei, J., Liu, M., Liu, L., Liu, Y., Wen, H., Tan, X., 2017. Sedimentary environment and sea level change of the subsalt interval of Member 5 of Ordovician Majiagou Formation in central Ordos Basin. J. Palaegeogr. 19, 773-790.
Xu, Y., Hu, X., Garzanti, E., Sun, G., Jiang, J., Li, J., Zhang, S., Schlagintweit, F., Rao, X., 2023.

Carbonate factories and their critical control on the geometry of carbonate platforms (mid-Cretaceous, southern Iran). Palaeogeography, Palaeoclimatology, Palaeoecology 625, 111680.

Yan, L., Li, H., Cao, Y., Yang, M., Zhao, Y., 2018. Revolution and segment characteristics of Cambrian carbonate platform margin in Manxi area,Tarim Basin. Nat. Gas. Geosci. 29, 807-816.

Yang, Z., Luo, P., Liu, B., Liu, C., Ma, J., Chen, F., 2017. The difference and sedimentation of two black rock series from Yurtus Formation during the earliest Cambrian in the Aksu area of Tarim Basin, Northwest China. Acta Petrol. Sin. 33, 1893-1918.

Ye, N., Li, Y., Liu, D., Xie, S., 2014. Sequence Stratigraphy of Cambrian in Tarim Basin. Xinjiang Geol. 32, 487-493.

Yoshida, S., Johnson, H.D., Pye, K., Dixon, R.J., 2004. Transgressive changes from tidal estuarine to marine embayment depositional systems: The Lower Cretaceous Woburn Sands of southern England and comparison with Holocene analogs. AAPG Bull. 88, 1433-1460.

Yu, B., Lin, C., Fan, T., Wang, L., Gao, Z., Zhang, C., 2011. Sedimentary response to geodynamic reversion in Tarim Basin during Cambrian and Ordovician and its significance to reservoir development. Earth Sci. Front. 18, 221-232.

Yu, J., Song, Y., Shi, K., Chen, S., Wang, Q., Liu, B., Han, J., 2022. Depositional facies and sequence architecture of the Yijianfang Formation in the Shuntuoguole Low Uplift, Tarim Basin, NW China. Geol. J. 57, 3135-3157.

Zadeh, P.G., Shafeii, A., 2021. Response of the Pliocene-Pleistocene carbonates to relative sea-level changes in Kish Island, Persian Gulf. J. Afr. Earth Sci. 183, 104316.

Zhang, J., Hu, M., Feng, Z., Li, Q., He, X., Zhang, B., Yan, B., Wei, G., Zhu, G., Zhang, Y., 2021. Types of the Cambrian platform margin mound-shoal complexes and their relationship with paleogeomorphology in Gucheng area, Tarim Basin, NW China. Petrol. Explor. Dev. 48, 94-105.

Zhang, X., Gao, Z., Maselli, V., Fan, T., 2023. Tectono-sedimentary characteristics and controlling factors of the lower-middle Cambrian gypsum-salt rocks in the Tarim Basin, Northwest China. Mar. Petrol. Geol. 151. 106189.

Zhang, Y., Chen, D., Zhou, X., Guo, Z., Wei, W., Mutti, M., 2015. Depositional facies and stratal cyclicity of dolomites in the Lower Qiulitag Group (Upper Cambrian) in northwestern Tarim Basin, NW China. Facies 61, 417.

Zhao, Z., 2015. Indicators of global sea-level change and research methods of marine tectonic sequences: take Ordovician of Tarim Basin as an example. Acta Petrol. Sin. 36, 262-273.

Zhao, Z., Luo, J., Zhang, Y., Wu, X., Pan, W., 2011. Lithofacies paleogeography of Cambrian sequences in the Tarim Basin. Acta Petrol. Sin. 32, 938-948.

Zhong, S., Tan, X., Hu, G., Nie, W., Yang, M., Zhang, D., Zheng, J., Xu, J., Dong, G., Xiao, D., Lu, Z., 2022. Control of paleogeographic pattern on sedimentary differentiation of evaporite-carbonate symbiotic system: A case study of the sixth sub-member of Ordovician Majiagou Formation M5 Member in central-eastern Ordos Basin, NW China. Petrol. Explor. Dev. 49, 837-850.

Zhou, X., Chen, D., Dong, S., Zhang, Y., Guo, Z., Wei, H., Yu, H., 2015. Diagenetic barite deposits in the Yurtus Formation in Tarim Basin, NW China: Implications for barium and sulfur cycling in the earliest Cambrian. Precambrian Res. 263, 79-87.

Zhu, D., Meng, Q., Jin, Z., Liu, Q., Hu, W., 2015. Formation mechanism of deep Cambrian dolomite reservoirs in the Tarim basin, northwestern China. Mar. Petrol. Geol. 59, 232-244.

Zhu, Y., Ni, X., Liu, L., Qiao, Z., Chen, Y., Zheng, J., 2019. Depositional Differentiation and Reservoir

Potential and Distribution of Ramp Systems during Post-rift Period: An example from the Lower Cambrian Xiaoerbulake Formation in the Tarim Basin,NW China. Acta Sed. Sin. 37, 1044-1057.
Zhuravlev, A.Y., Wood, R.A., 2018. The two phases of the Cambrian Explosion. Sci. Rep. 8, 16656.

Fig. 1. Study area is shown. (a) Location of the Tarim Basin in China. (b) Map of the major tectonic units and the Middle Cambrian paleogeography of Tarim Basin. Modified from Lin et al. (2011) and Wei et al. (2021). The location of the study area is indicated. Note the locations of the studied wells: 1- Y1, 2- Y2, 3- Y3, 4- Y4, 5- Y5.

Fig. 2. Seismic profile of Line 1 (shown in Fig. 1b). The division of sequence stratigraphic elements of the rimmed carbonate platform margin and the distribution of facies is not clear from seismic data before the study. T_9^0, the bottom of the Lower Cambrian; T_8^1, the top of the Middle Cambrian; T_8^0, the top of the Upper Cambrian.

Fig. 3. Schematic illustration of the regional Cambrian lithostratigraphic successions and correlation between the platform interior zone, the platform margin zone and the basin zone of the Tarim Basin. Modified from (Jiang et al., 2021a; Jiang et al., 2021b; Zhao et al., 2011).

Table 1 Description of microfacies types and microfacies associations of the Middle and Lower Cambrian in the Tabei Uplift of Tarim Basin. Abbreviations: A, abundant; F, frequent; C, less common; R, rare; N/A, none or absent

Fig. 4. Photomicrographs of characteristic features of microfacies MF1-MF9b under PPL: (a) PPL photomicrographs of Argillite (MF1) in well Y2, ∈1y, 8647m; (b) PPL photomicrographs of Argillaceous limestone (MF2) in well Y1, ∈1y, 8746m; (c) PPL photomicrographs of Micitic limestone (MF3) in well Y4, ∈1y, 8315m; (d) PPL photomicrographs of Peloid packstone (MF4) in well Y1, ∈1x, 8687m; (e) PPL photomicrographs of Intraclast grainstone (MF5a) in well Y1, ∈1x, 8340m; (f) PPL photomicrographs of Rudstone (MF5b) in well Y1, ∈1x, 8261m; (g) PPL photomicrographs of Ooid grainstone (MF5c) in well Y2, ∈1x, 8230m; (h) PPL photomicrographs of Dolomitic limestone (MF6) in well Y1, ∈1x, 8242.68m; (i) PPL photomicrographs of Calcareous dolomite (MF7) in well Y1, ∈1x, 8431m; (j) PPL photomicrographs of Argillaceous dolomite (MF8) in well Y1, ∈1w, 8130m; (k) Micitic dolomite (MF9a) in well Y4, □2a, 7664m; (l) PPL photomicrographs of Finely crystalline dolomite (MF9b) in well Y4, □2s, 7827m.

Fig. 5. Photomicrographs of characteristic features of microfacies MF9c-MF16 under PPL: (a) PPL photomicrographs of Medium-coarse crystalline dolomite (MF9c) in well Y4, □1w, 8094m; (b) PPL photomicrographs of Peloid dolo-packstone (MF10) in well Y5, ∈2a, 8312m; (c) PPL photomicrographs of Intraclast dolo wackstone (MF11) in well Y4, □1w, 8039m; (d) PPL photomicrographs of Ooid dolo-grainstone (MF12a) in well Y4, □2s, 7738m; (e) PPL

photomicrographs of Intraclast dolo-grainstone (MF12b) in well Y5, □2a, 8227m; (f) PPL photomicrographs of Residual intraclast dolomite (MF13) in well Y4, □2a, 7418m; (g) PPL photomicrographs of Thrombolite dolomite (MF14a) in well Y5, □2a, 7772m; (h) PPL photomicrographs of Strombolite dolomite (MF14b) in well Y4, □2a, 7659m; (i) PPL photomicrographs of Foam spongy dolomite (MF14c) in well Y4, □2a, 7578m; (j) PPL photomicrographs of Oncoid dolomite (MF14d) in well Y4, □2a, 7640m; (k) PPL photomicrographs of Gypsum dolomite (MF15) in well Y1, □2a, 7966m; (l) PPL photomicrographs of Anhydrite (MF16) in well Y1, □2a, 7942m.

Fig. 6. Seven microfacies associations (MA1-MA7) inferred to have developed in shelf and ramp settings. (a) Variant distribution and relative abundance of microfacies types in different microfacies associations are indicated. Facies transition trends and depositional environments are shown; (b-h) Main meter-scale depositional cycles developed in different microfacies associations: b- Deep shelf (widespread in the Yuertusi Formation), c- Shallow shelf (widespread in the Yuertusi Formation), d- Outer ramp (present in well Y4 in the Lower Cambrian), e- Outer middle ramp (widespread in the Xiaoerbulake Formation), f- Inner middle ramp (present in well Y1 in the Xiaoerbulake Formation), g- Lagoon of middle ramp (present in well Y1 in the Xiaoerbulake Formation), h- Shoal of middle ramp (present in well Y2 in the Xiaoerbulake Formation).

Fig. 7. The seven microfacies associations (MA8-MA14) inferred to have developed in carbonate platform setting. (a) Variant distribution and relative abundance of microfacies types in different microfacies associations are indicated, facies transition trends and depositional environments are shown; (b-h) Main meter-scale depositional cycles developed in different microfacies associations: b- Muddy dolomite flat (present in well Y1 in the Wusongeer Formation and Middle Cambrian), c- dolomite flat (present in well Y3, Y4 and Y5 in the Wusongeer Formation and Middle Cambrian, d- gypsum dolomite flat (present in well Y1 and Y2 in the Wusongeer and Awatage formations), e- Shoal inner platform (present in well Y4 and Y5 in the Formation), f- Mound inner platform (present in well Y4 and Y5 in the Formation), g- Margin mound-shoal complex (present in well Y2, Y3,Y4 and Y5 in the Wusongeer Formation and Middle Cambrian), h- Margin shoal (present in well Y3,Y4 and Y5 in the Wusongeer Formation and Middle Cambrian).

Fig. 8. Schematic summary of microfacies, depositional environments, sequence stratigraphic framework, Fischer plot, geochemical signatures and relative sea-level change of Lower and Middle Cambrian in well Y1. The sampling interval of the cuttings is 2 m. The relative sea-level change curve is reconstructed based on microfacies, geochemical characteristics and Fischer plot. RST1, regressive systems tract of Sq1; MFS, maximum flooding surface; TST1, transgressive systems tract.

Fig. 9. Schematic summary of microfacies, depositional environments, sequence stratigraphic framework, Fischer plot, geochemical signatures and relative sea-level change of Lower and Middle

Cambrian in well Y2. The sampling interval of the cuttings is 5 m. The relative sea-level change curve is reconstructed based on microfacies, geochemical characteristics and Fischer plot. RST1, regressive systems tract of Sq1; MFS, maximum flooding surface; TST1, transgressive systems tract.

Fig. 10. Schematic summary of microfacies, depositional environments, sequence stratigraphic framework, Fischer plot, geochemical signatures and relative sea-level change of Lower and Middle Cambrian in well Y4. The sampling interval of the cuttings is 2 m. The relative sea-level change curve is reconstructed based on microfacies, geochemical characteristics and Fischer plot. RST1, regressive systems tract of Sq1; MFS, maximum flooding surface; TST1, transgressive systems tract.

Fig. 11. Seismic facies identified in the present study, and associated interpretations of the depositional environment in the Cambrian succession.

Fig. 12. Interpreted seismic profile of line 2 (see location on Fig. 1b), revealing the pattern of Ediacaran rift inside and outside the platform, as well as its control on Cambrian sedimentation.

Fig. 13. Un-interpreted (a), and interpreted (b, c) seismic profiles of Line 3 in the study area (see location on Fig. 1b), showing the geomorphic pattern of the Cambrian platform margin in Lower and Middle Cambrian.

Fig. 14. Correlation of depositional facies within the sequence stratigraphic framework of Lower Cambrian in the Tabei Uplift, Tarim Basin, exhibiting the spatiotemporal facies variations within third-order depositional sequences.

Fig. 15. Correlation of depositional facies within the sequence stratigraphic framework of Middle Cambrian in the Tabei Uplift, Tarim Basin, exhibiting the spatiotemporal facies variations within third-order depositional sequences.

Fig. 16. Principle and example of Fischer plot. (a) Initial Fischer plot (modified from Fischer (1964)). Vertical axis is the accommodation space, and abscissa axis is the time. (b) Improved Fischer plot. The vertical axis is the cumulative deviation of average thickness, which means accumulation of D-value between each cycle's thickness and the average cycle thickness, abscissa axis is the number of cycles (Sadler et al., 1993). (c) Interpretation of Fischer plot in Middle Cambrian, well Y5. Fischer plot indicates periodic increases and decreases.

Table 2 Statistics of high-frequency cycles cycle data of different wells in the Tabei Uplift area in the Lower-Middle Cambrian.

Fig. 17. Correlation of paleo-water depth changes in the Tabei Uplift in the Lower-Middle Cambrian

with the global sea-level curve constructed by (Haq and Schutter, 2008).

Fig. 18. Depositional evolution pattern of microfacies of the Lower Cambrian platform in the Tabei Uplift, Tarim Basin. (a) broad shelf depositional pattern during Sq1-Sq2 period; (b) Distal steepening ramp depositional pattern during Sq3-Sq4 period; (c) Distal steepening ramp transforming to weakly rimmed platform depositional pattern during Sq5 period. Sq1–Sq5, third-order depositional sequence 1–5. RST, regressive systems tract; TST, transgressive systems tract.

Fig. 19. Depositional evolution pattern and the of the Middle Cambrian platform in the Tabei Uplift, Tarim Basin. (a) Rimmed Platform depositional pattern during Sq6 (TST6) period; (b) Strongly rimmed platform depositional pattern during Sq6 (RST6)-Sq8 period. Sq6–Sq8, third-order depositional sequence 6–8. RST, regressive systems tract; TST, transgressive systems tract.

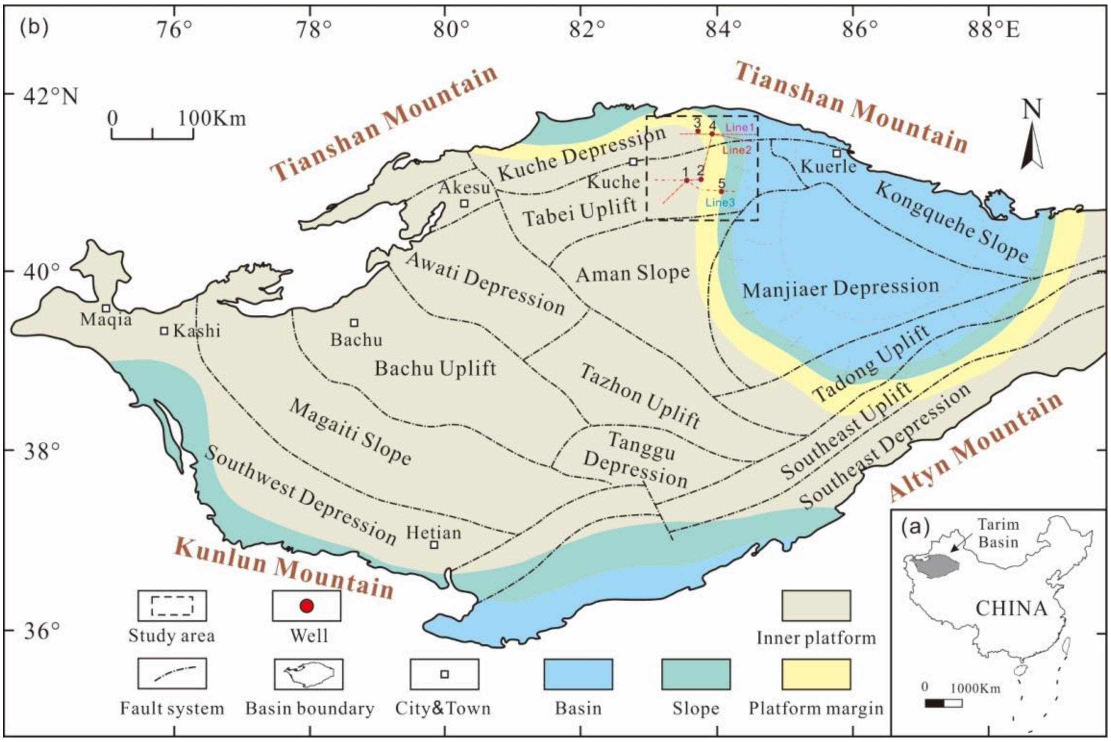

Fig. 1. Study area is shown. (a) Location of the Tarim Basin in China. (b) Map of the major tectonic units and the Middle Cambrian paleogeography of Tarim Basin. Modified from Lin et al. (2011) and Wei et al. (2021). The location of the study area is indicated. Note the locations of the studied wells: 1- Y1, 2- Y2, 3- Y3, 4- Y4, 5- Y5.

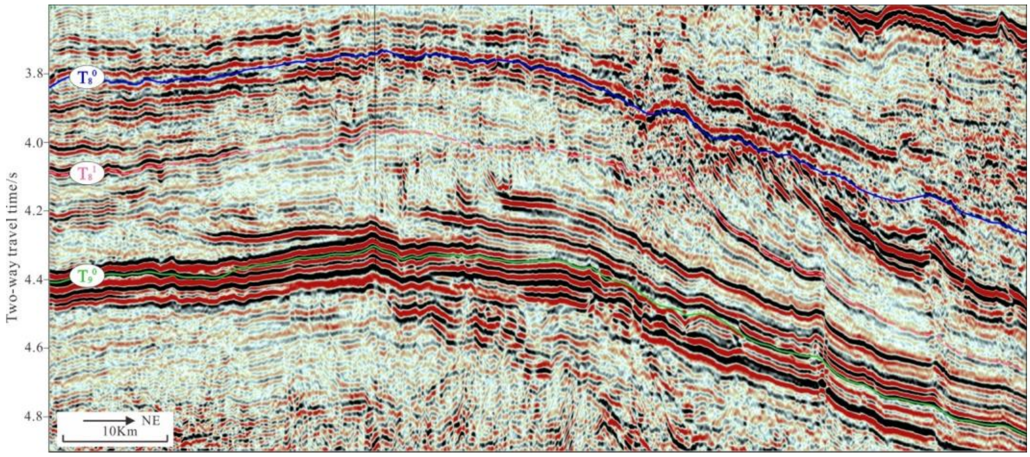

Fig. 2. Seismic profile of Line 1 (shown in Fig. 1b). The division of sequence stratigraphic elements of the rimmed carbonate platform margin and the distribution of facies is not clear from seismic data before the study. T_9^0, the bottom of the Lower Cambrian; T_8^1, the top of the Middle Cambrian; T_8^0, the top of the Upper Cambrian.

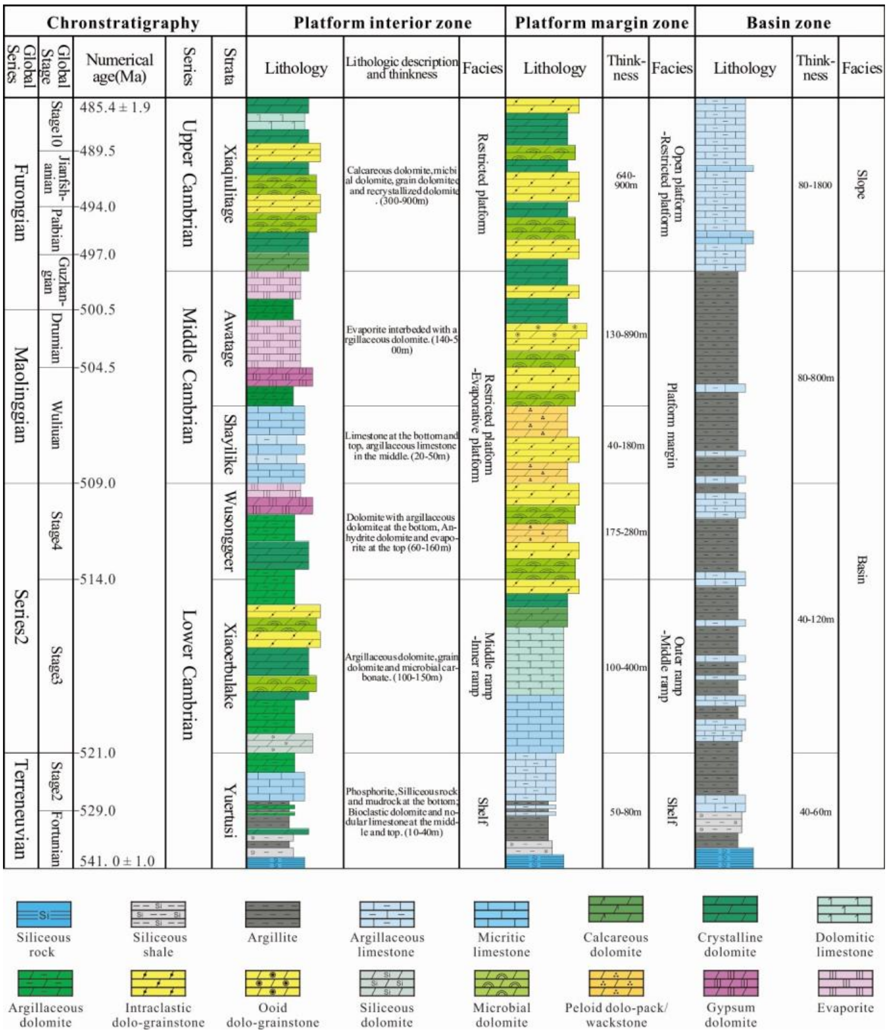

Fig. 3. Schematic illustration of the regional Cambrian lithostratigraphic successions and correlation between the platform interior zone, the platform margin zone and the basin zone of the Tarim Basin. Modified from (Jiang et al., 2021a; Jiang et al., 2021b; Zhao et al., 2011).

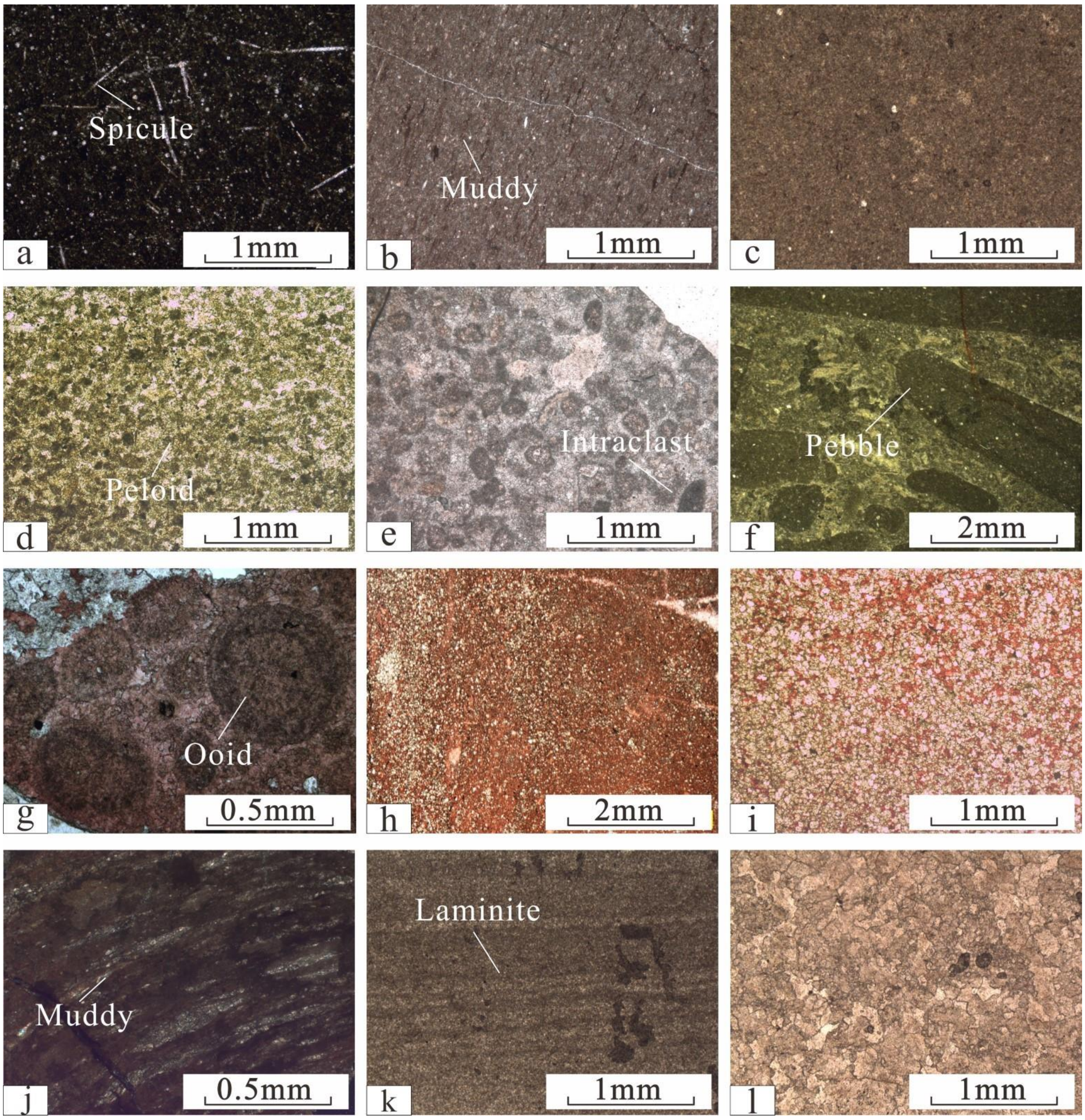

Fig. 4. Photomicrographs of characteristic features of microfacies MF1-MF9b under PPL: (a) PPL photomicrographs of Argillite (MF1) in well Y2, ∈1y, 8647m; (b) PPL photomicrographs of Argillaceous limestone (MF2) in well Y1, ∈1y, 8746m; (c) PPL photomicrographs of Micitic limestone (MF3) in well Y4, ∈1y, 8315m; (d) PPL photomicrographs of Peloid packstone (MF4) in well Y1, ∈1x, 8687m; (e) PPL photomicrographs of Intraclast grainstone (MF5a) in well Y1, ∈1x, 8340m; (f) PPL photomicrographs of Rudstone (MF5b) in well Y1, ∈1x, 8261m; (g) PPL photomicrographs of Ooid grainstone (MF5c) in well Y2, ∈1x, 8230m; (h) PPL photomicrographs of Dolomitic limestone (MF6) in well Y1, ∈1x, 8242.68m; (i) PPL photomicrographs of Calcareous dolomite (MF7) in well Y1, ∈1x, 8431m; (j) PPL photomicrographs of Argillaceous dolomite (MF8) in well Y1, ∈1w, 8130m; (k) Micitic dolomite (MF9a) in well Y4, ∈2a, 7664m; (l) PPL photomicrographs of Finely crystalline dolomite (MF9b) in well Y4, ∈2s, 7827m.

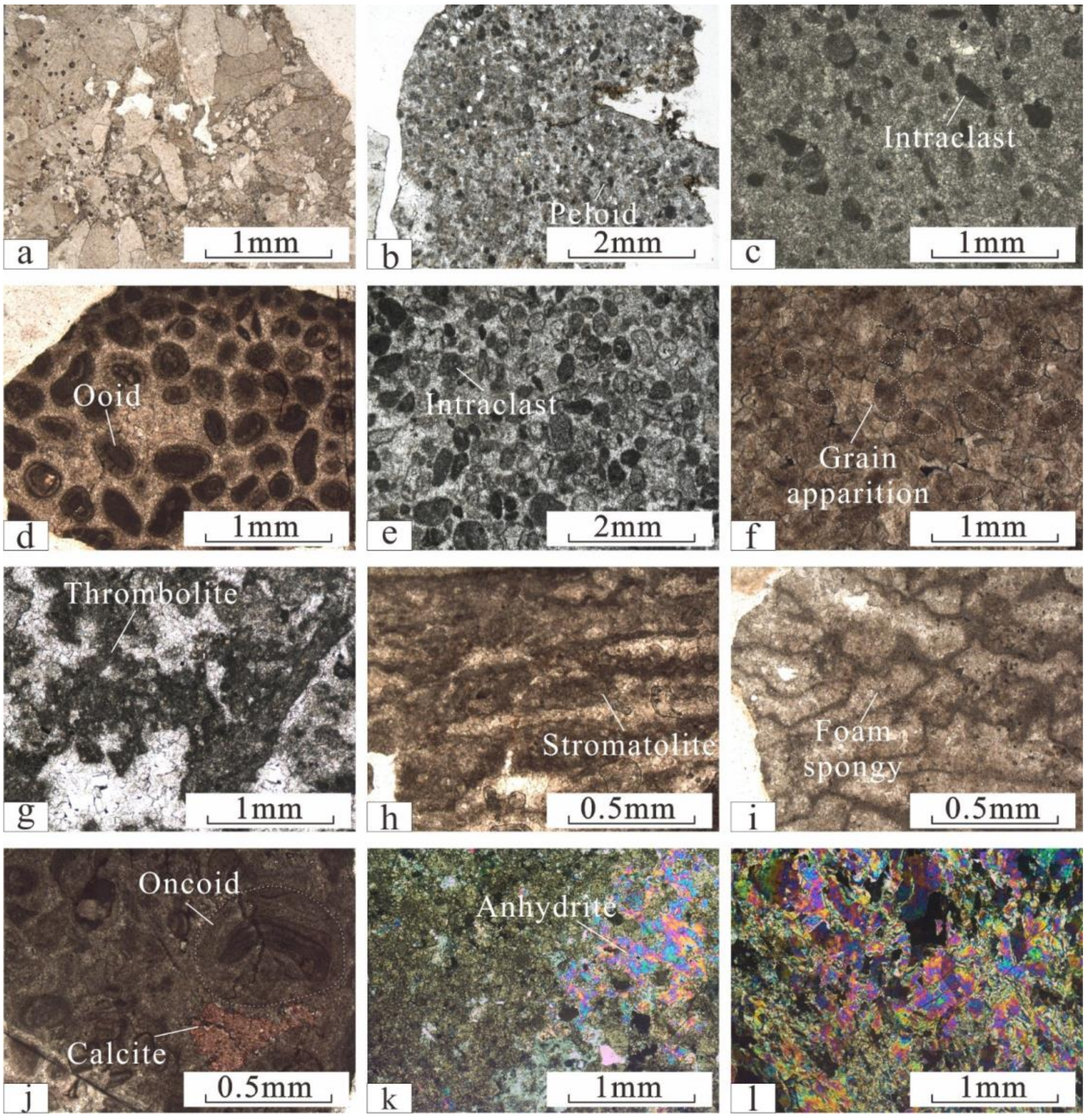

Fig. 5. Photomicrographs of characteristic features of microfacies MF9c-MF16 under PPL: (a) PPL photomicrographs of Medium-coarse crystalline dolomite (MF9c) in well Y4, ∈1w, 8094m; (b) PPL photomicrographs of Peloid dolo-packstone (MF10) in well Y5, ∈ 2a, 8312m; (c) PPL photomicrographs of Intraclast dolo wackstone (MF11) in well Y4, ∈1w, 8039m; (d) PPL photomicrographs of Ooid dolo-grainstone (MF12a) in well Y4, ∈2s, 7738m; (e) PPL photomicrographs of Intraclast dolo-grainstone (MF12b) in well Y5, ∈2a, 8227m; (f) PPL photomicrographs of Residual intraclast dolomite (MF13) in well Y4, ∈2a, 7418m; (g) PPL photomicrographs of Thrombolite dolomite (MF14a) in well Y5, ∈2a, 7772m; (h) PPL photomicrographs of Strombolite dolomite (MF14b) in well Y4, ∈2a, 7659m; (i) PPL photomicrographs of Foam spongy dolomite (MF14c) in well Y4, ∈2a, 7578m; (j) PPL photomicrographs of Oncoid dolomite (MF14d) in well Y4, ∈2a, 7640m; (k) PPL photomicrographs of Gypsum dolomite (MF15) in well Y1, ∈2a, 7966m; (l) PPL photomicrographs of Anhydrite (MF16) in well Y1, ∈2a, 7942m.

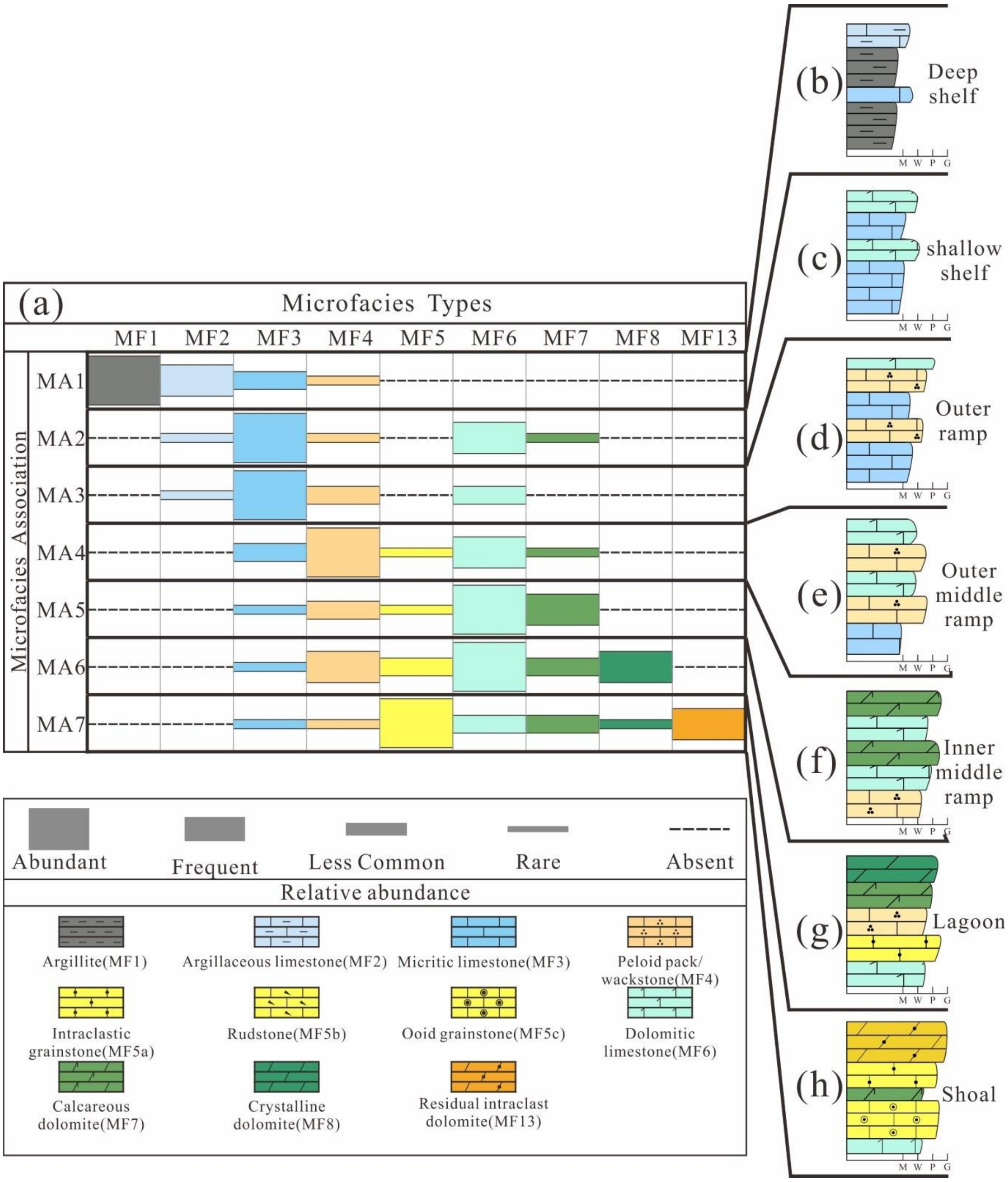

Fig. 6. Seven microfacies associations (MA1-MA7) inferred to have developed in shelf and ramp settings. (a) Variant distribution and relative abundance of microfacies types in different microfacies associations are indicated. Facies transition trends and depositional environments are shown; (b-h) Main meter-scale depositional cycles developed in different microfacies associations: b- Deep shelf (widespread in the Yuertusi Formation), c- Shallow shelf (widespread in the Yuertusi Formation), d- Outer ramp (present in well Y4 in the Lower Cambrian), e- Outer middle ramp (widespread in the Xiaoerbulake Formation), f- Inner middle ramp (present in well Y1 in the Xiaoerbulake Formation), g- Lagoon of middle ramp (present in well Y1 in the Xiaoerbulake Formation), h- Shoal of middle ramp (present in well Y2 in the Xiaoerbulake Formation).

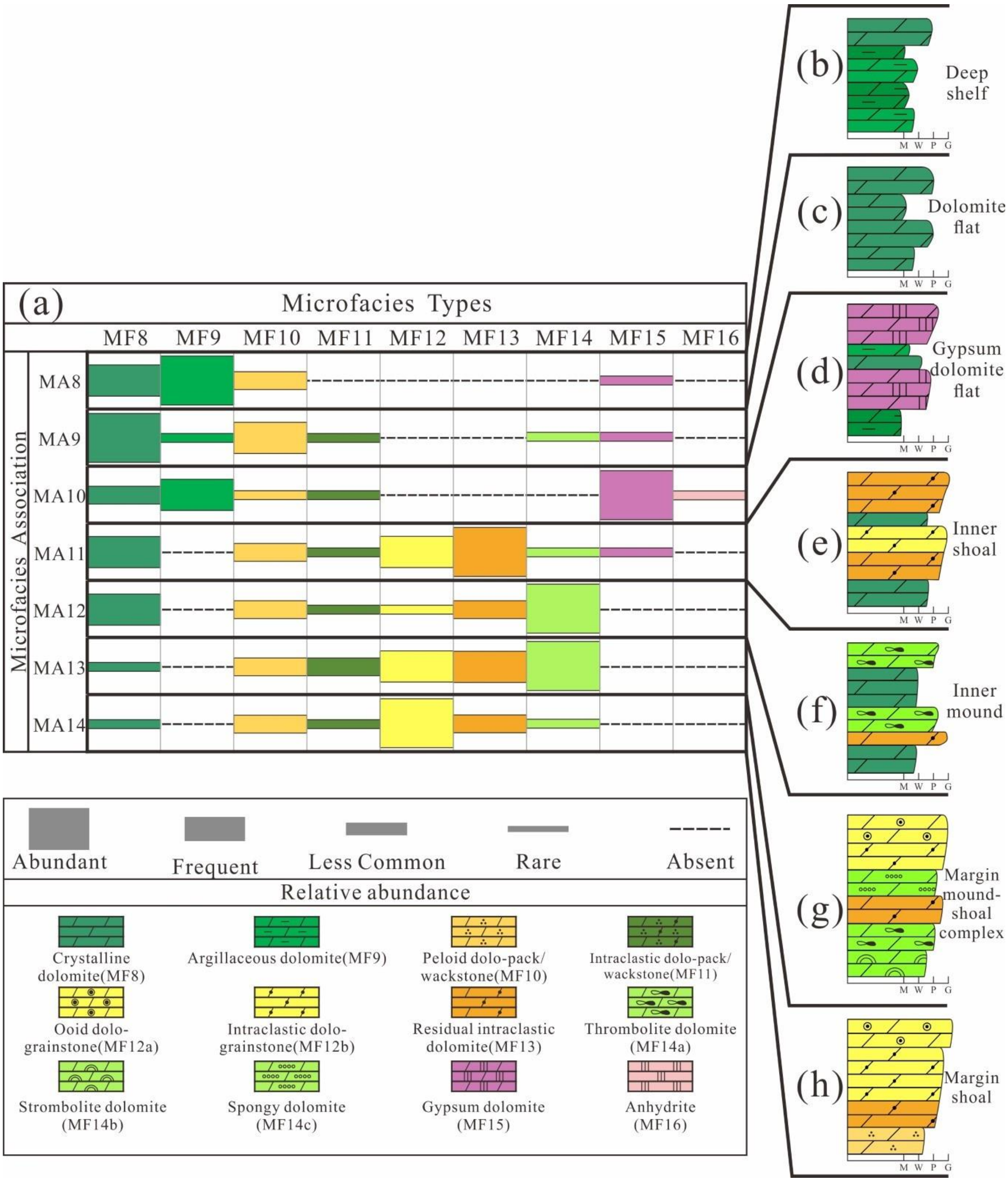

Fig. 7. The seven microfacies associations (MA8-MA14) inferred to have developed in carbonate platform setting. (a) Variant distribution and relative abundance of microfacies types in different microfacies associations are indicated, facies transition trends and depositional environments are shown; (b-h) Main meter-scale depositional cycles developed in different microfacies associations: b- Muddy dolomite flat (present in well Y1 in the Wusongeer Formation and Middle Cambrian), c- dolomite flat (present in well Y3, Y4 and Y5 in the Wusongeer Formation and Middle Cambrian, d- gypsum dolomite flat (present in well Y1 and Y2 in the Wusongeer and Awatage formations), e- Shoal inner platform (present in well Y4 and Y5 in the Formation), f- Mound inner platform (present in well Y4 and Y5 in the Formation), g- Margin mound-shoal complex (present in well Y2, Y3,Y4 and Y5 in the Wusongeer Formation and Middle Cambrian), h- Margin shoal (present in well Y3,Y4 and Y5 in the Wusongeer Formation and Middle Cambrian).

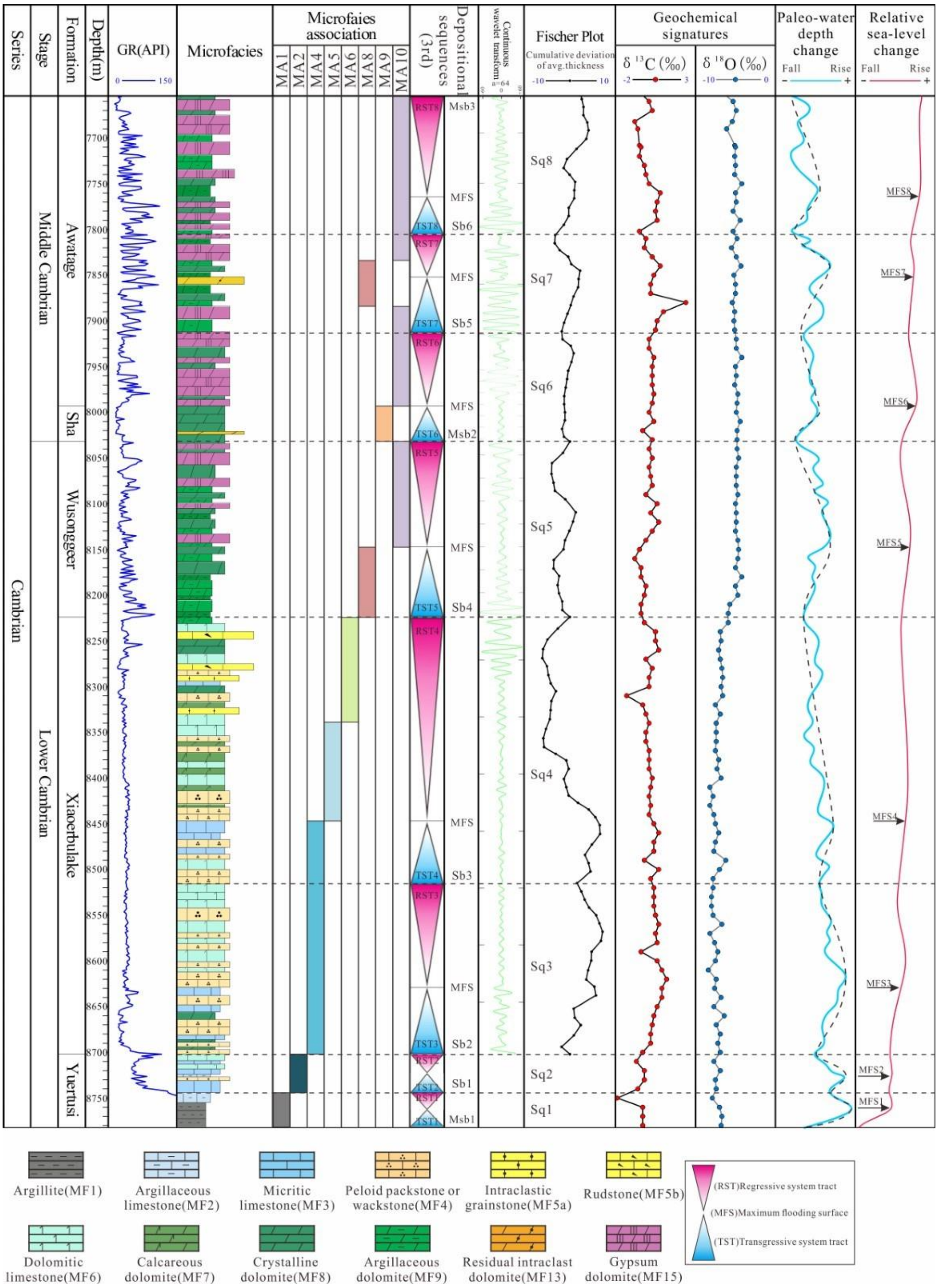

Fig. 8. Schematic summary of microfacies, depositional environments, sequence stratigraphic framework, Fischer plot, geochemical signatures and relative sea-level change of Lower and Middle Cambrian in well Y1. The sampling interval of the cuttings is 2 m. The relative sea-level change curve is reconstructed based on microfacies, geochemical characteristics and Fischer plot. RST1, regressive systems tract of Sq1; MFS, maximum flooding surface; TST1, transgressive systems tract.

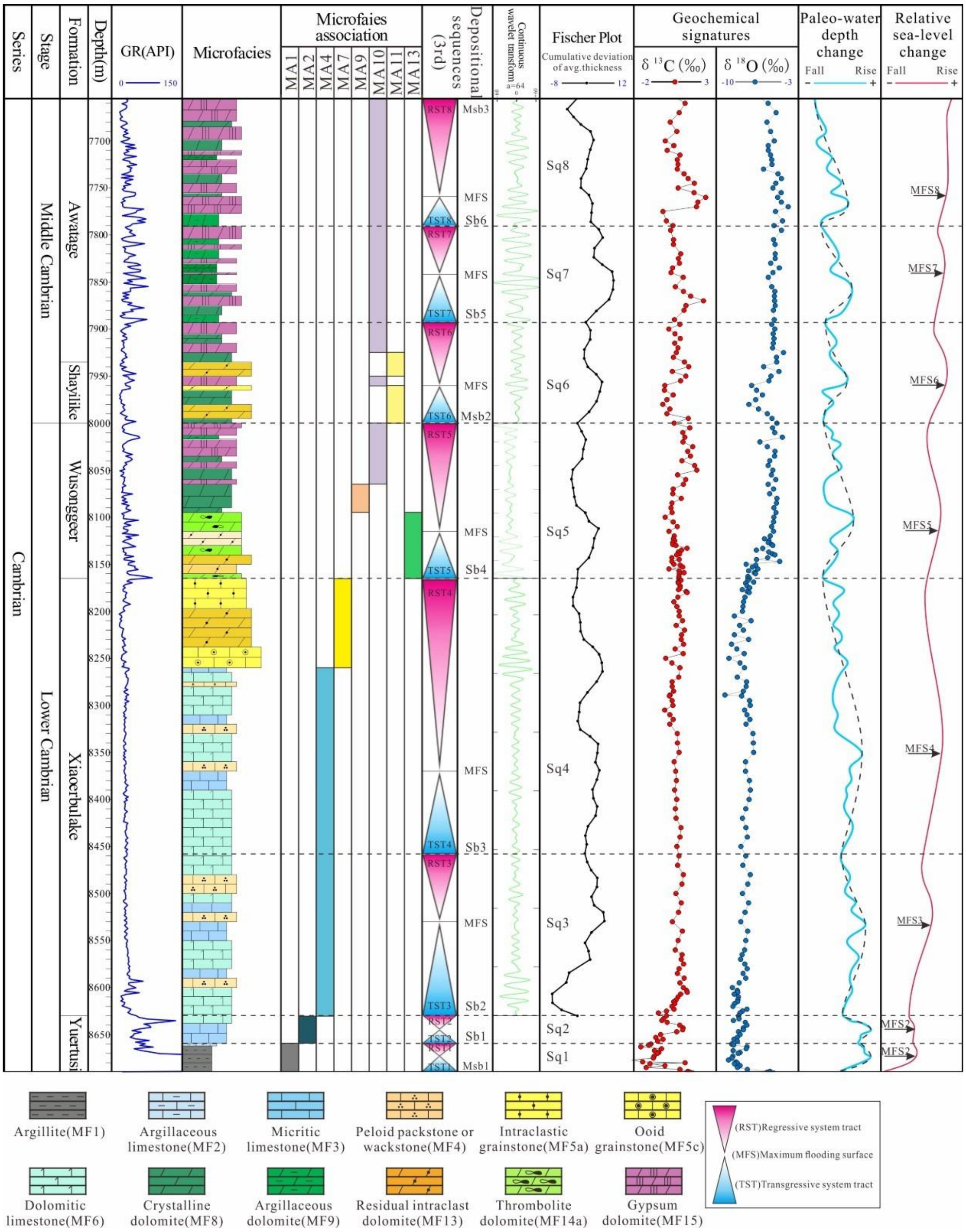

Fig. 9. Schematic summary of microfacies, depositional environments, sequence stratigraphic framework, Fischer plot, geochemical signatures and relative sea-level change of Lower and Middle Cambrian in well Y2. The sampling interval of the cuttings is 5 m. The relative sea-level change curve is reconstructed based on microfacies, geochemical characteristics and Fischer plot. RST1, regressive systems tract of Sq1; MFS, maximum flooding surface; TST1, transgressive systems tract.

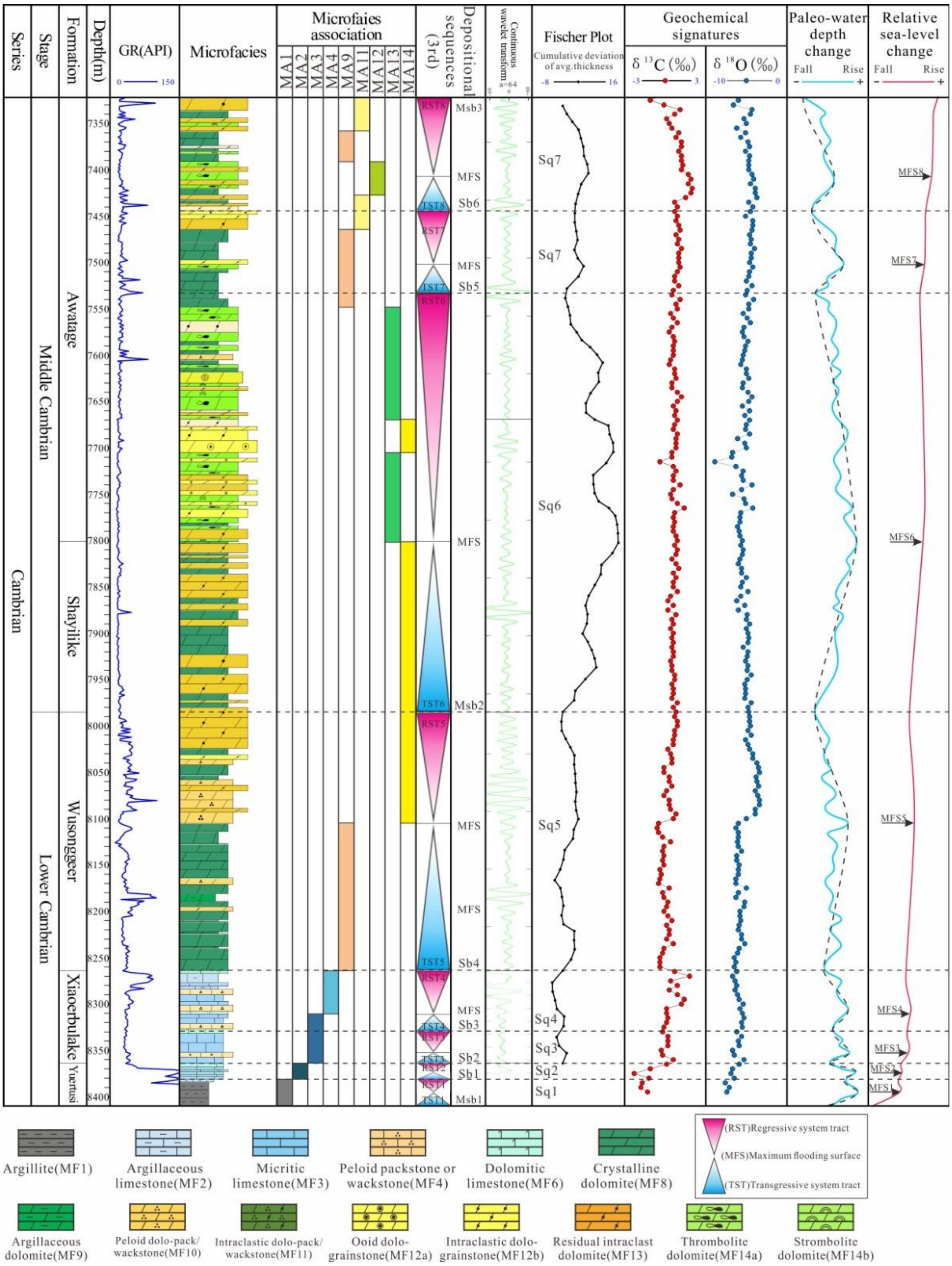

Fig. 10. Schematic summary of microfacies, depositional environments, sequence stratigraphic framework, Fischer plot, geochemical signatures and relative sea-level change of Lower and Middle Cambrian in well Y4. The sampling interval of the cuttings is 2 m. The relative sea-level change curve is reconstructed based on microfacies, geochemical characteristics and Fischer plot. RST1, regressive systems tract of Sq1; MFS, maximum flooding surface; TST1, transgressive systems tract.

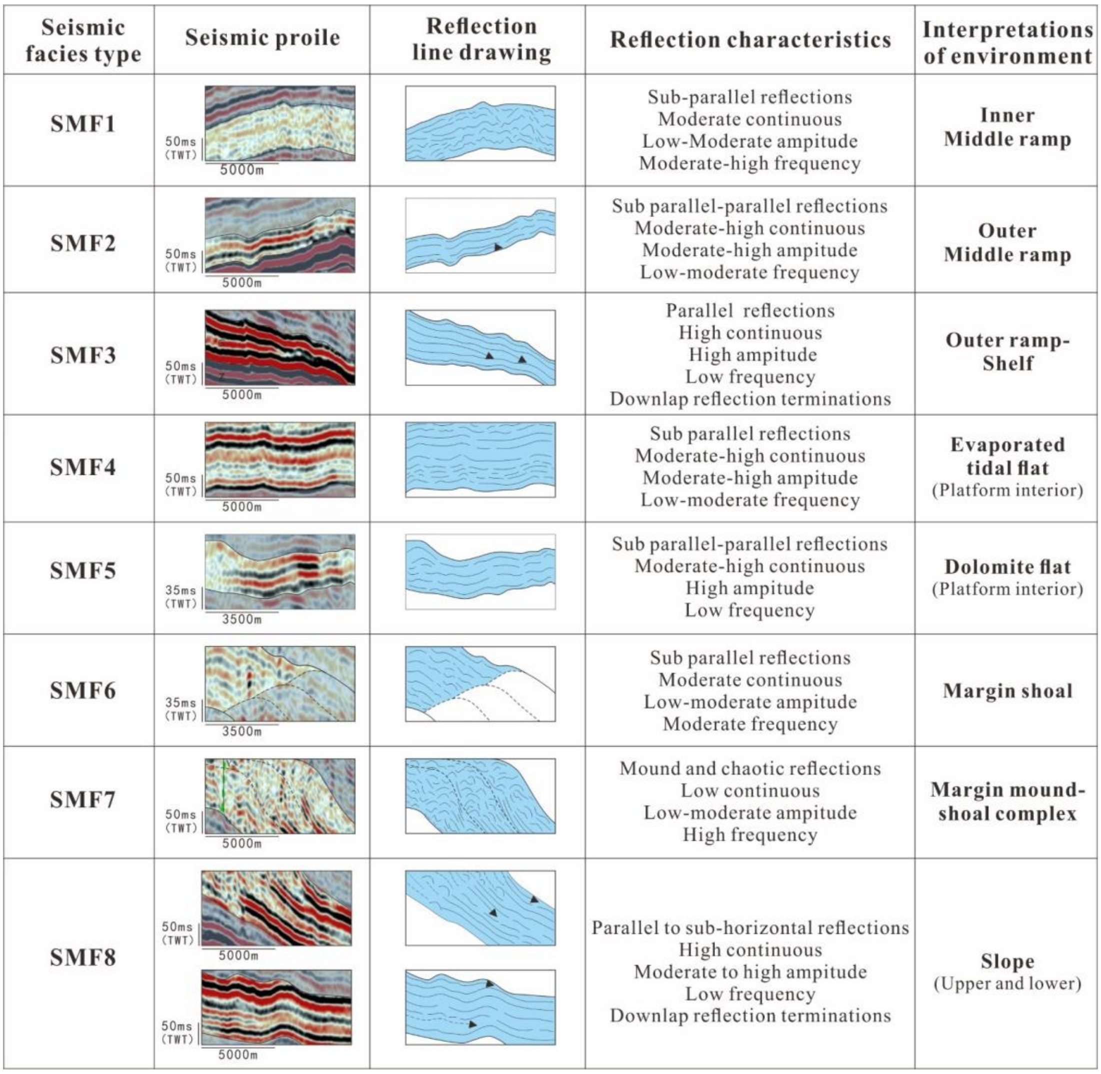

Fig. 11. Seismic facies identified in the present study, and associated interpretations of the depositional environment in the Cambrian succession.

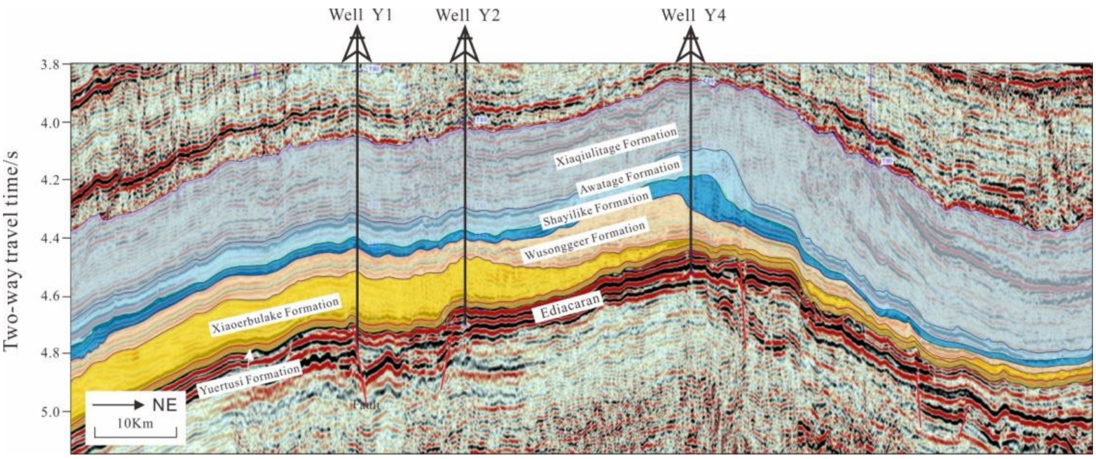

Fig. 12. Interpreted seismic profile of line 2 (see location on Fig. 1b), revealing the pattern of Ediacaran rift inside and outside the platform, as well as its control on Cambrian sedimentation.

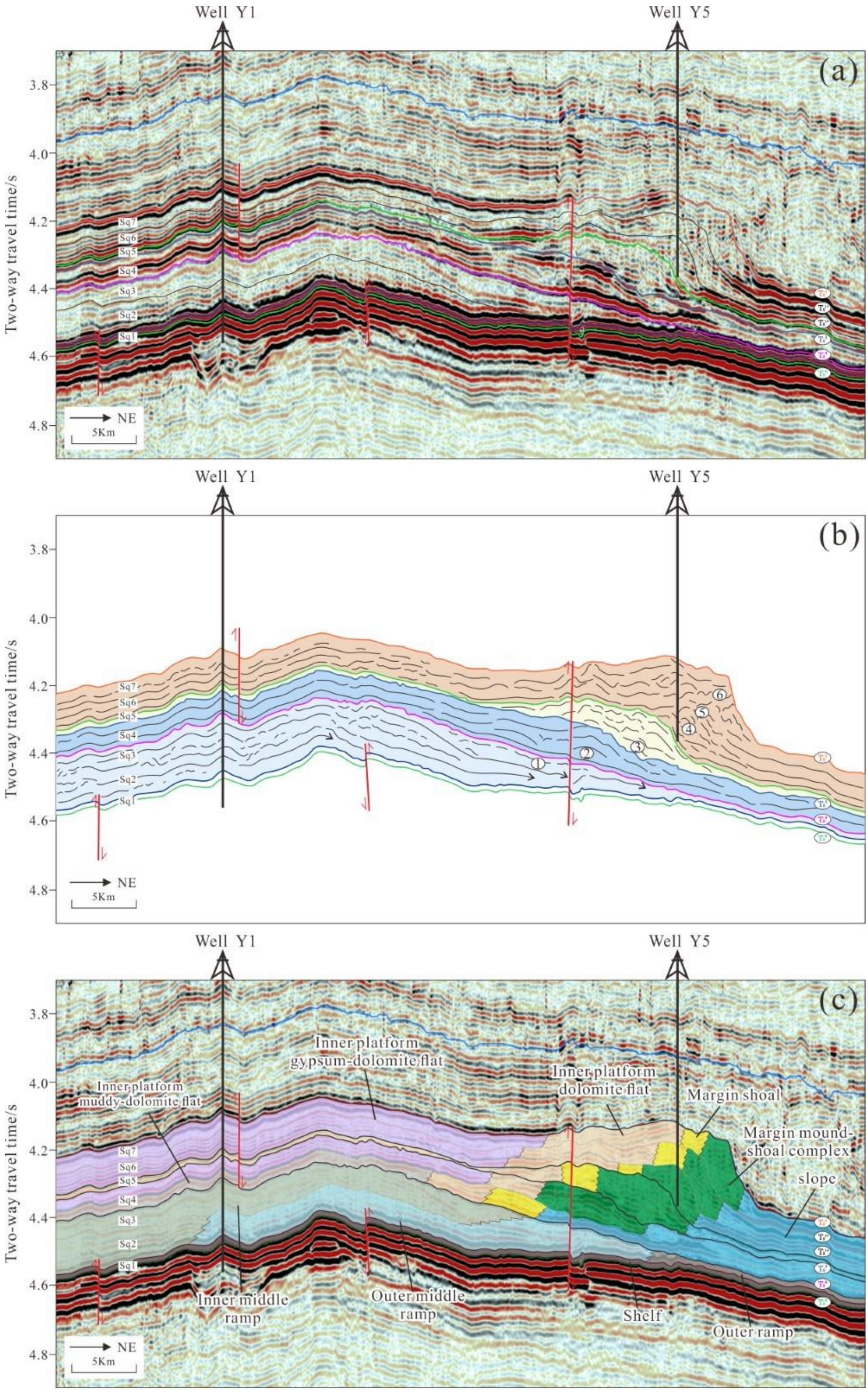

Fig. 13. Un-interpreted (a), and interpreted (b, c) seismic profiles of Line 3 in the study area (see location on Fig. 1b), showing the geomorphic pattern of the Cambrian platform margin in Lower and Middle Cambrian.

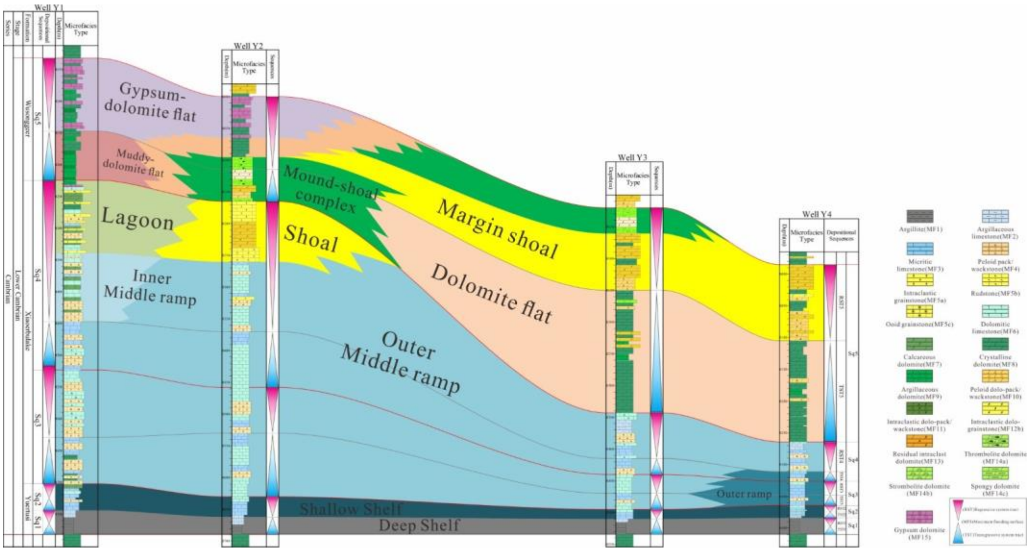

Fig. 14. Correlation of depositional facies within the sequence stratigraphic framework of Lower Cambrian in the Tabei Uplift, Tarim Basin, exhibiting the spatiotemporal facies variations within third-order depositional sequences.

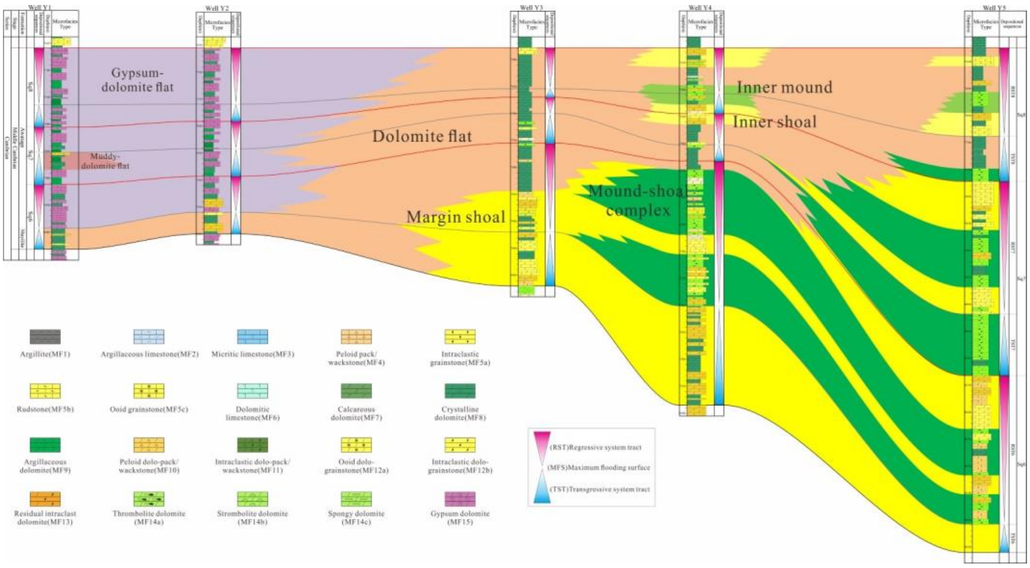

Fig. 15. Correlation of depositional facies within the sequence stratigraphic framework of Middle Cambrian in the Tabei Uplift, Tarim Basin, exhibiting the spatiotemporal facies variations within third-order depositional sequences.

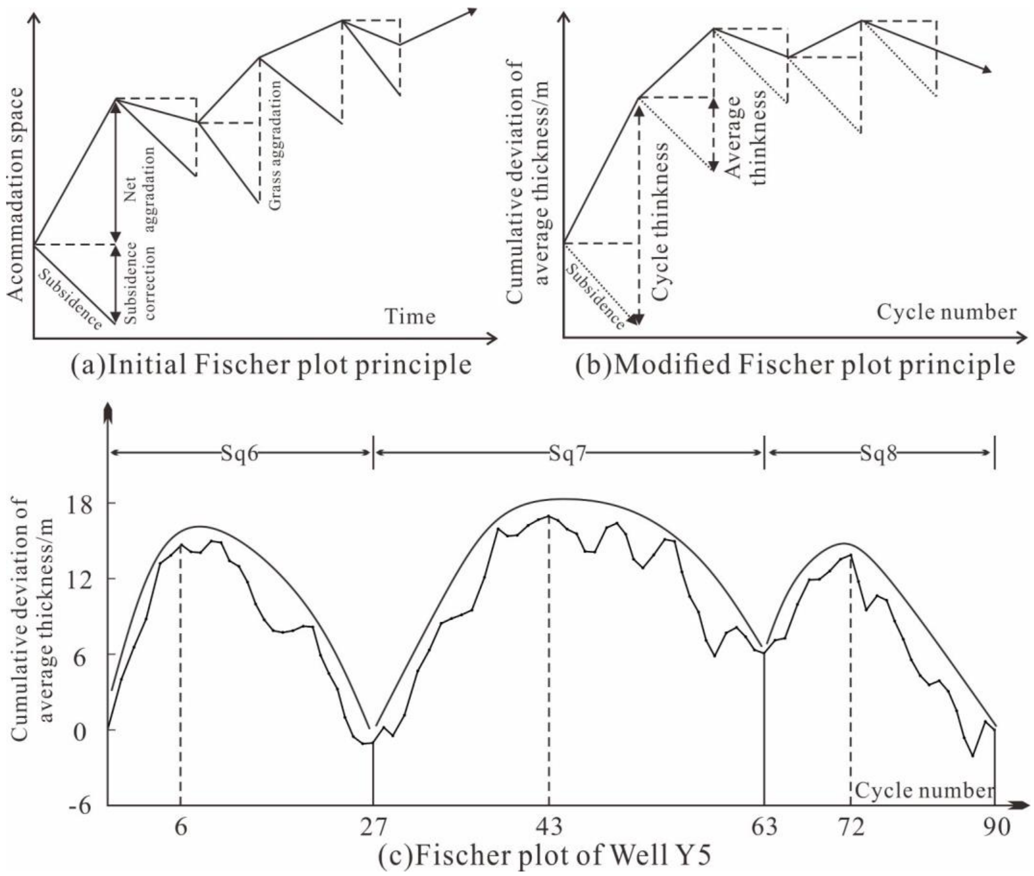

Fig. 16. Principle and example of Fischer plot. (a) Initial Fischer plot (modified from Fischer (1964)). Vertical axis is the accommodation space, and abscissa axis is the time. (b) Improved Fischer plot. The vertical axis is the cumulative deviation of average thickness, which means accumulation of D-value between each cycle's thickness and the average cycle thickness, abscissa axis is the number of cycles (Sadler et al., 1993). (c) Interpretation of Fischer plot in Middle Cambrian, well Y5. Fischer plot indicates periodic increases and decreases.

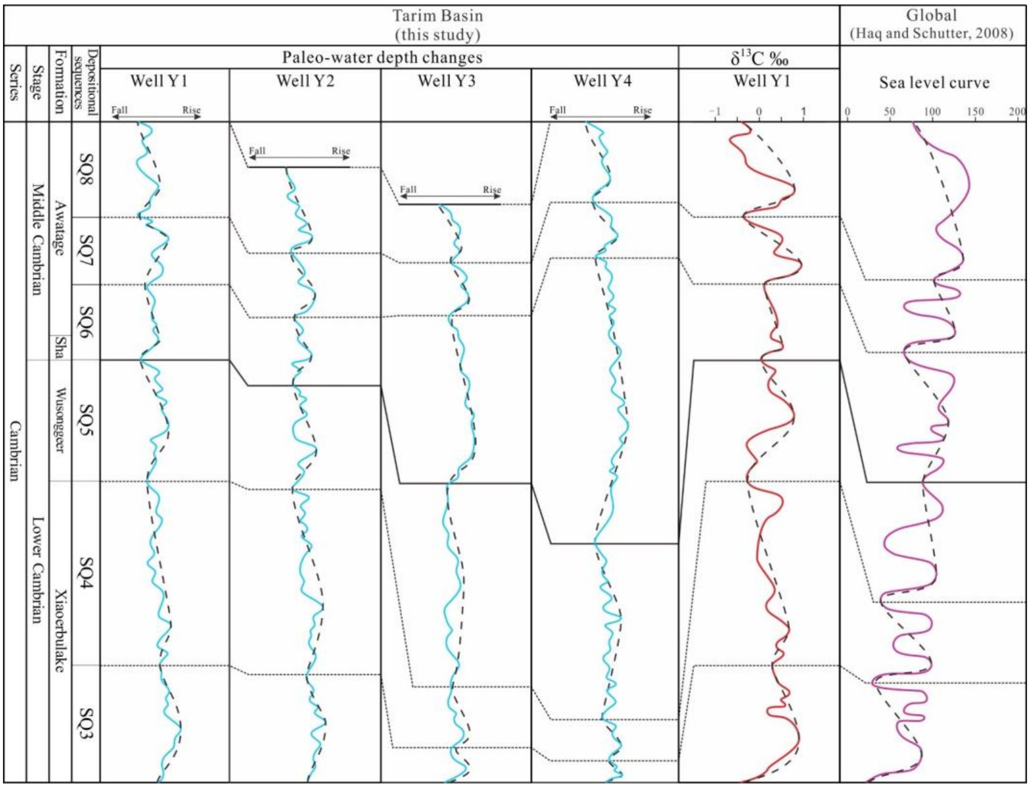

Fig. 17. Correlation of paleo-water depth changes in the Tabei Uplift in the Lower-Middle Cambrian with the global sea-level curve constructed by (Haq and Schutter, 2008).

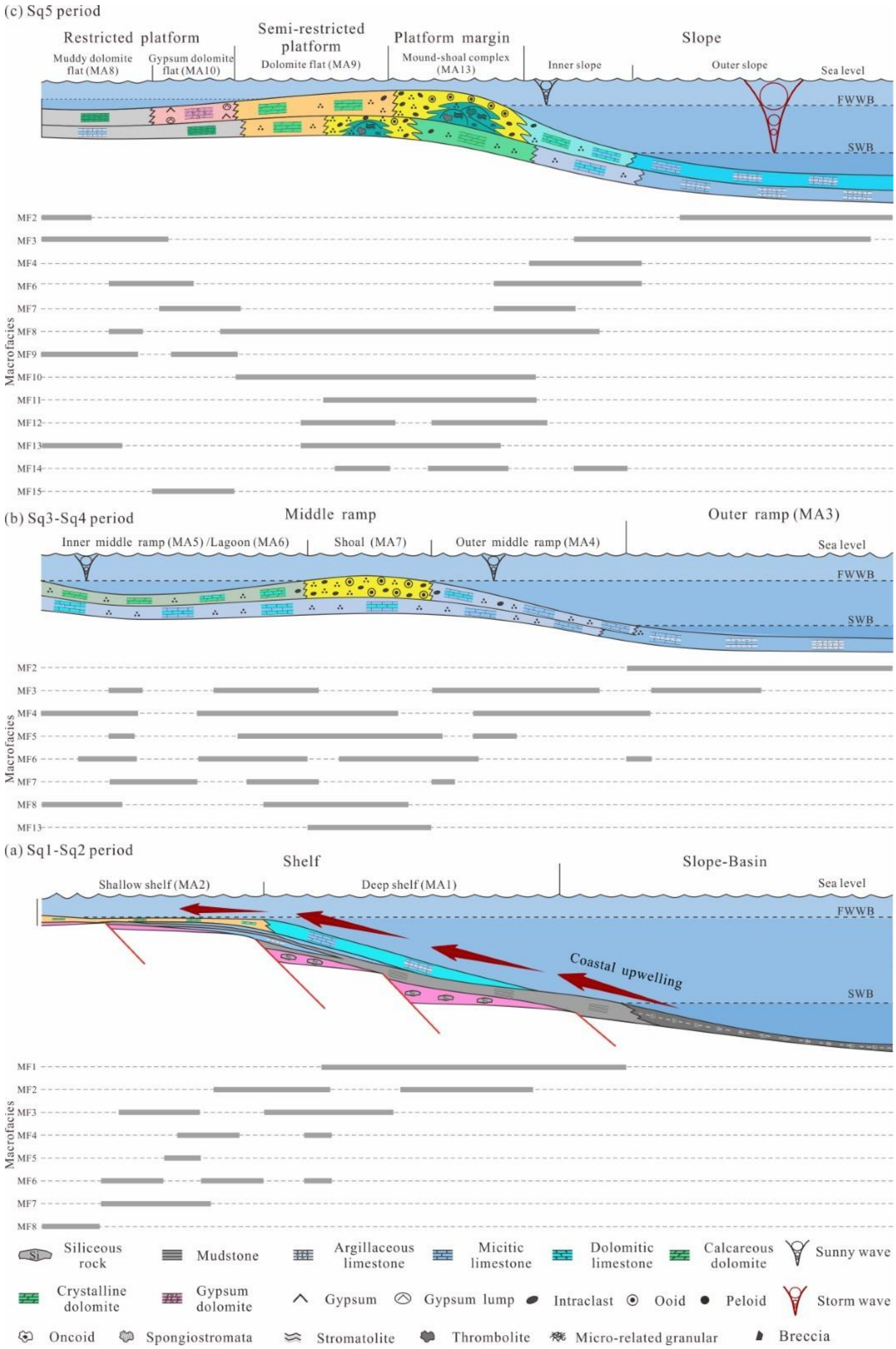

Fig. 18. Depositional evolution pattern of microfacies of the Lower Cambrian platform in the Tabei Uplift, Tarim Basin. (a) broad shelf depositional pattern during Sq1-Sq2 period; (b) Distal steepening ramp depositional pattern during Sq3-Sq4 period; (c) Distal steepening ramp transforming to weakly rimmed platform depositional pattern during Sq5 period. Sq1–Sq5, third-order depositional sequence 1–5. RST, regressive systems tract; TST, transgressive systems tract.

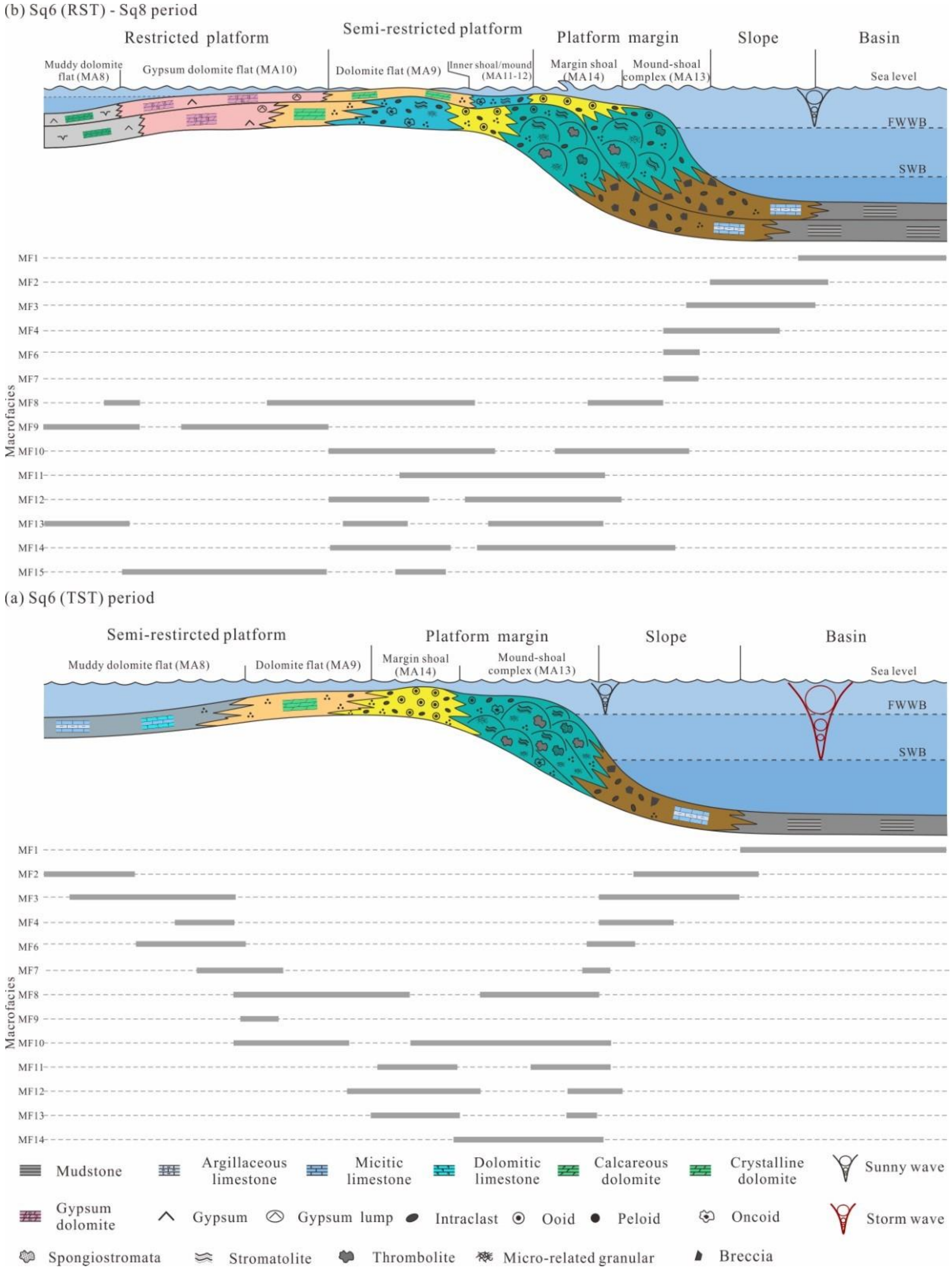

Fig. 19. Depositional evolution pattern and the of the Middle Cambrian platform in the Tabei Uplift, Tarim Basin. (a) Rimmed Platform depositional pattern during Sq6 (TST6) period; (b) Strongly rimmed platform depositional pattern during Sq6 (RST6)-Sq8 period. Sq6–Sq8, third-order depositional sequence 6–8. RST, regressive systems tract; TST, transgressive systems tract.

Table 1.

Microfacies code	Microfacies name	Description	Composition 1- Non-bioclasts; 2- Bioclasts	Depositional Environment Energy	Relative abundance in different microfacies associations
MF1	Argillite	Black color; high organic matter content; contain much siliceous spicule; widely presents in the study area at the bottom of the Cambrian	1-micrite (R) 2-spicule (A)	Low energy	MA1 (A)
MF2	Argillaceous limestone	Dark grey color; fine laminated texture; composite with some argillaceous material; locally contorted or slump folded (soft sediment deformation structure); rare spicule can be observed; widespreads laterally in the study area and overlay by MF1	1- micrite (A) 2-spicule (R)	Low energy	MA1 (F); MA2 (R); MA3 (R)
MF3	Micritic limestone	Light grey to gray color; calcite in composition; exhibited by fine lamination with alternation of mud rich lamina and widespreads in the Yuertusi and Xiaoerbulake Formation in the study area	1- micrite (A) 2-peloid (R)	Low energy	MA1 (C); MA2 (A); MA3 (A); MA4 (C); MA5 (R); MA6 (R); MA7 (R)
MF4	Peloid pack/wackstone	Grey to dark grey color; moderately sorted; peloids are very fine–fine (50–100 μm); partial calcite; peloid with a content of 20%-50%; matrix or grain-supported; partial calcite recrystallization; widespreads in the Xiaoerbulake Formation in the study area	1-peloid (A); micrite (F) 2-trilobite (C)	Moderate-low energy	MA1 (R); MA2 (R); MA3 (C); MA4 (A); MA5 (C); MA6 (F); MA7 (R)
MF5a	Intraclast grainstone	Grey color; intraclasts are fine–middle (100-500μm) and can be divided into conglomerate, sand and silt size; poorly-moderately sorted; grains are primarily intraclasts a content of 50%-70%; partial calcite recrystallization; grain-supported; only presents on the top of the Xiaoerbulake Formation in well Y1 and Y2	1-intralcast (A); peloid (C) 2-trilobite (R)	High energy	MA4 (R); MA5 (R); MA6 (F); MA7 (F)
MF5b	Rudstone	Light grey to grey color;	1-pebble (A);	High energy	MA5 (R); MA6 (F);

		poorly sorted; grains are primarily pebbleconglomerate-sized intraclasts; coarse (1-2.5mm) grain-supported; intergranular pore spaces cemented by calcite; only presents on the top of the Xiaoerbulake Formation in well Y1	peloid (R) 2- trilobite (R)		MA7 (R)
MF5c	Ooid grainstone	Grey color; moderately well sorted; ooids are fine-middle (200-400μm) and can be divided into conglomerate and sand size; contains concentric layer structure; grain-supported and the intergrain is cemented by sparry calcite with fine bright crystalline; only presents on the top of the Xiaoerbulake Formation in well Y2	1-ooid (A) 2- trilobite (N/A)	High energy	MA6 (C); MA7 (A)
MF6	Dolomitic limestone	Gray color; partial calcite recrystallization; dolomite scattered distribution; calcite with a content of 15%-25%; weak lamination; vugs filled with sparry calcite with fine bright crystalline; widespreads in the Xiaoerbulake Formation in the study area	1-micrite (A); peloid (R) 2-Bioclasts (N/A)	Low energy	MA2 (F); MA3 (C);MA4 (F); MA5 (A); MA6 (A); MA7 (C)
MF7	Calcareous dolomite	Dark grey color; calcite undergo dolomitization into very finely crystalline structure; calcite with a content of 25%-50%; vugs filled with sparry calcite with fine bright crystalline; widespreads in the Xiaoerbulake Formation in wells Y1, Y2 and Y3	1-very finely crystalline (A); peloid (R) 2-Non	Low energy	MA2 (R); MA4 (R); MA5 (F); MA6 (C); MA7 (C)
MF8a	Micritic-very finely crystalline dolomite	Dark grey; micritic-very fine crystalline structure; rare laminar development with rich muddy; mainly presents in the Wusonggeer and Awatage formations in wells Y1 and Y2	1-micrite-very finely crystalline (A); argillaceous (R) 2- Bioclasts (N/A)	Low energy	MA6 (F); MA7 (R); MA8 (F); MA9 (C); MA10 (C)
MF8b	Finely crystalline dolomite	Grey color; fine crystal structure and the crystals are 100-250μm and without any relict texture; show semi-planar to nonplanar texture; widespreads in the Wusonggeer Formation and	1- finely crystalline (A) 2- Bioclasts (N/A)	Moderate-low energy	MA6 (R); MA8 (R); MA9 (A); MA10 (C); MA11 (F); MA12 (F); MA13 (R); MA14 (R)

		the Middle Cambrian succession in the study area			
MF8c	Middle-coarsely crystalline dolomite	Light gray color; middle-coarse crystal structure, crystals are 250-1000 μm, show planar to semi-planar texture; original component and structure are no longer recognisable without any relict texture; only presents in the Awatage Formation in wells Y4 and Y5	1-middle-coarsely crystalline (A) 2-Non	Moderate energy	MA9 (F) MA11 (C); MA12 (C)
MF9	Argillaceous dolomite	Dark gray to black color; contains argillaceous laminated stripes; slump folded (soft sediment deformation structure); only presents in the Shayilike and Awatage formations in wells Y1 and Y2 and overlay by MF9a	1-micrite (A); argillaceous (F) 2- Bioclasts (N/A)	Low energy	MA8 (A); MA9 (R); MA10 (F)
MF10	Peloid dolo-pack/wackstone	Gery color; moderately-sorted, peloids are very fine–fine (50–100 μm); peloid with a content of 20%-50%; matrix or grain-supported; mainly presents in the Wusonggeer Formation and Middle Cambrian succession in wells Y3, Y4 and Y5	1-peloid (A); micrite (F) 2- Bioclasts (R)	Moderate-low energy	MA8 (C); MA9 (F); MA10 (R); MA11 (F); MA12 (C); MA13 (C); MA14 (C)
MF11	Intraclastic dolo-pack/wackstone	Gery color; the dominant grains are silt-sized (50-200μm) intraclast with a content of 20-40%; The components are minor filaments of bacteria and algae; poorly sorted; matrix or grain-supported; mainly presents in the Middle Cambrian succession in wells Y3, Y4 and Y5	1-intraclast (A); peloid (C) 2-Bioclasts (R)	Moderate energy	MA9 (R); MA10 (R); MA11 (R); MA12 (R); MA13 (C); MA14 (R)
MF12a	Ooid dolo-grainstone	Light grey; ooids are fine-middle (200-500μm) and can be divided into conglomerate and sand size; moderately to well sorted, contains concentric layer structure; grain-supported and the intergrain is cemented by fine crystalline sparry dolomite; mainly presents in the Middle Cambrian succession in wells	1-ooid (A); intraclast (C) 2- Bioclasts (N/A)	High energy	MA11 (R); MA12 (R); MA13 (C); MA14 (C)

		Y4 and Y5			
MF12b	Intraclast dolo-grainstone	Light grey to grey color; intraclasts are fine–middle (200-500μm) and can be divided into conglomerate and sand and silt size; poorly to moderately sorted; grain-supported and the intergrain is cemented by fine crystalline sparry dolomite; mainly presents in the Wusonggeer and the Middle Cambrian succession in wells Y3, Y4 and Y5	1- intraclast (A); peloid (C) 2- Bioclasts (R)	High energy	MA11 (C); MA12 (R); MA13 (C); MA14 (A)
MF13	Residual intraclast dolomite	Light grey color; intraclast is replaced by fine to medium crystalline dolomite with obvious graining lines; the crystalline dolomite is characterized by cloudy at the cente and bright around the edges; fine-middle crystal structure; mainly presents in the Wusonggeer and the Middle Cambrian succession in wells Y2, Y3, Y4 and Y5	1-finely-middle crystalline (A); intraclast (R) 2- Bioclasts (R)	Moderate-low energy	MA11 (A); MA12 (C); MA13 (F); MA14 (C)
MF14a	Thrombolite dolomite	Dark grey to grey color; poorly sorted; clotted structure; microbial frameworks are cemented by very fine crystalline sparry dolomite; mainly presents in the Wusonggeer and the Middle Cambrian succession in wells Y2, Y3, Y4 and Y5	1-micrite (F) 2-thrombolite (A)	Moderate-low energy	MA11 (R); MA12 (F); MA13 (A); MA14 (R)
MF14b	Strombolite dolomite	Dark grey to grey color; laminated structure; interactive development of light and dark laminae; develops hummocky or flower - shaped lamina; mainly presents in the Middle Cambrian succession in wells Y3, Y4 and Y5	1-micrite (F) 2-strombolite (A)	Moderate-low energy	MA9 (R); MA11 (R); MA12 (C); MA13 (F);
MF14c	Foam spongy dolomite	Dark grey to grey color; Foam spongy structure; sizes of the spongy frameworks are different and are cemented with sparry dolomite; mainly presents in the Awatage Formation in wells Y4 and Y5	1-micrite (F) 2-spongy (A)	High energy	MA11 (R); MA12 (R); MA13 (C);
MF14d	Oncoidal dolomite	Grey color; oncoids are fine-middle in size (200-500μm);	1-micrite (F); ooid (R)	High energy	MA11 (R); MA12 (R); MA13 (R);

		microbial bonding structure inside oncoids; poorly to moderately sorted; grain-supported with fine crystalline sparry dolomite; mainly presents in the Awatage Formation in wells Y4 and Y5	2-oncoid (A)		MA14 (R)
MF15	Gypsum dolomite	Light grey and grey color; filled with the shape of chicken wire and sausage; dolomite is dominated by micritic crystalline with little content of very fine crystalline dolomite; mainly presents in the Wusonggeer and Awatage formations in wells Y1 and Y2	1-micrite (A); gypsum (C) 2-Bioclasts (N/A)	Low energy	MA8 (R); MA9 (R); MA10 (A); MA11 (R);
MF16	Anhydrite	Brownish grey to brown color; single crystal structure with cluster distribution characteristics; only presents in the Awatage formations in wells Y1 and Y2	1-crystalline gypsum (A) 2-Bioclasts (N/A)	Low energy	MA10 (R)

Table 2.

Well	Stratigraphy	Total thickness	Cycle number	Average cycle thickness	Max cycle thickness	Min cycle thickness	Microfacies associations
Y1	Sq3-Sq5	670m	69	9.7m	14.6m	6.7m	MA4, MA5, MA6, MA8, MA10
	Sq6-Sq8	378m	47	8.9m	11.3m	7.0m	MA8, MA9, MA10
Y3	Sq3-Sq5	473m	49	9.7m	12.9m	5.8m	MA4, MA9, MA13, MA14
	Sq6-Sq8	442m	47	9.4m	13.0m	6.7m	MA9, MA14
Y2	Sq3-Sq5	630m	67	9.5m	13.9m	6.2m	MA4, MA7, MA9, MA10, MA13
	Sq6-Sq8	345.5m	36	9.8m	13.6m	7.5m	MA10, MA11
Y4	Sq3-Sq5	379m	38	10.0m	12.8m	7.2m	MA3, MA4, MA9, MA14
	Sq6-Sq8	663m	66	9.9m	13.2m	6.5m	MA9, MA11, MA12, MA13, MA14
Y5	Sq6-Sq8	884m	90	9.8m	14.2m	7.4m	MA9, MA11, MA12, MA13, MA14